Cell

TULIPs decorate the three-dimensional genome of PFA ependymoma

Graphical abstract

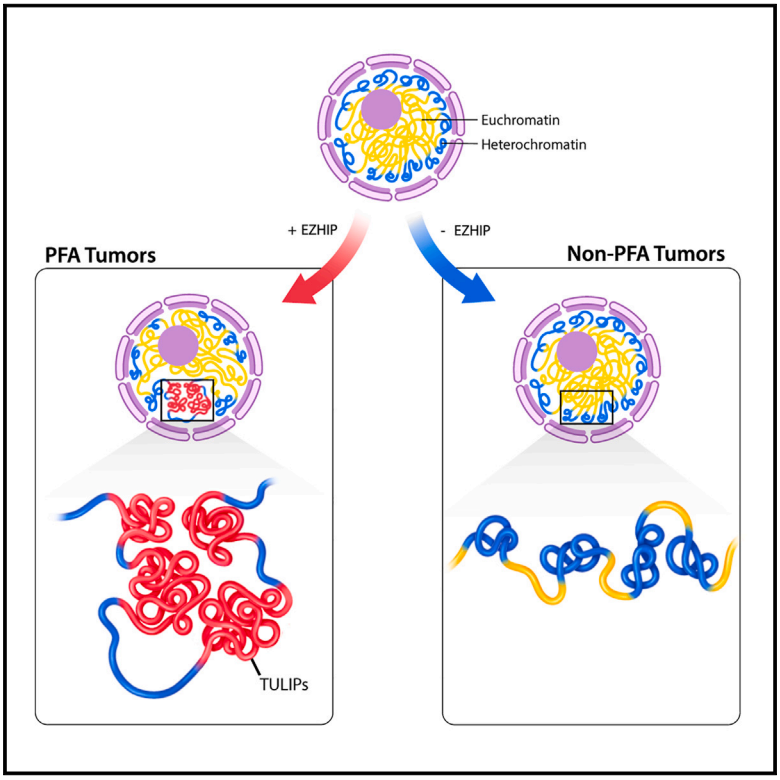

Authors

Michael J. Johnston, John J.Y. Lee, Bo Hu, ..., Nada Jabado, Michael D. Taylor, Marco Gallo

Correspondence

nada.jabado@mcgill.ca (N.J.), michael.taylor@bcm.edu (M.D.T.), marco.gallo@bcm.edu (M.G.)

In brief

Comparative 3D genome studies of childhood brain tumors identified TULIPs, highly recurrent topological features that are characteristic of PFA ependymoma.

Highlights

- The 3D genome of PFA ependymoma is reminiscent of stem-like cell types
- TULIPs are recurrent 3D genome structures unique to PFA
- TULIPs form strong long-range interactions between H3K9me3^{+} regions
- EZHIP reorganizes chromatin architecture to produce TULIPs

Johnston et al., 2024, Cell *187*, 1–20
September 5, 2024
https://doi.org/10.1016/j.cell.2024.06.023

CellPress

Cell

CellPress
OPEN ACCESS

Article

TULIPs decorate the three-dimensional genome of PFA ependymoma

Michael J. Johnston,[1,2,38] John J.Y. Lee,[3,4,5,38] Bo Hu,[6,7,38] Ana Nikolic,[1,2,9,38] Elham Hasheminasabgorji,[1,2,9] Audrey Baguette,[10] Seungil Paik,[1,2] Haifen Chen,[6] Sachin Kumar,[7] Carol C.L. Chen,[6] Selin Jessa,[10] Polina Balin,[3,4,5] Vernon Fong,[3,4,5] Melissa Zwaig,[6] Kulandaimanuvel Antony Michealraj,[7] Xun Chen,[8] Yanlin Zhang,[11] Srinidhi Varadharajan,[12] Pierre Billon,[1,9] Nikoleta Juretic,[13] Craig Daniels,[3,4] Amulya Nageswara Rao,[14] Caterina Giannini,[14] Eric M. Thompson,[15] Miklos Garami,[16] Peter Hauser,[16] Timea Pocza,[16] Young Shin Ra,[17] Byung-Kyu Cho,[18] Seung-Ki Kim,[18] Kyu-Chang Wang,[18] Ji Yeoun Lee,[18]

(Author list continued on next page)

[1]Arnie Charbonneau Cancer Institute, Cumming School of Medicine, University of Calgary, Calgary, AB T2N 4N1, Canada
[2]Alberta Children's Hospital Research Institute, Cumming School of Medicine, University of Calgary, Calgary, AB T2N 4N1, Canada
[3]The Arthur and Sonia Labatt Brain Tumor Research Center, The Hospital for Sick Children, Toronto, ON M5G 0A4, Canada
[4]Developmental & Stem Cell Biology Program, The Hospital for Sick Children, Toronto, ON M5G 0A4, Canada
[5]Department of Laboratory Medicine and Pathobiology, University of Toronto, Toronto, ON M5G 1L7, Canada
[6]Department of Human Genetics, McGill University, Montreal, QC H2A 1B1, Canada
[7]Department of Neurological Surgery, University of Pittsburgh School of Medicine, Pittsburgh, PA 15213, USA
[8]Department of Anatomy and Cell Biology, Kyoto University, Kyoto 606-8501, Japan
[9]Department of Biochemistry and Molecular Biology, Cumming School of Medicine, University of Calgary, Calgary, AB T2N 4N1, Canada
[10]Quantitative Life Sciences, McGill University, Montreal, QC H3A 1B9, Canada
[11]School of Computer Science, McGill University, Montreal, QC H3A 2A7, Canada
[12]Department of Developmental Neurobiology, St Jude Children's Research Hospital, Memphis, TN 38105, USA
[13]Department of Pediatrics, McGill University and The Research Institute of the McGill University Health Centre, Montreal, QC H4A 3J1, Canada
[14]Pediatric Hematology-Oncology, Mayo Clinic, Rochester, MN 55905, USA
[15]Department of Neurosurgery, Duke University Medical Center, Durham, NC 27710, USA
[16]Department of Pediatrics, Semmelweis University, H-1094 Budapest, Hungary
[17]Department of Neurosurgery, University of Ulsan, Asan Medical Center, Seoul 05505, South Korea
[18]Department of Neurosurgery, Division of Pediatric Neurosurgery, Seoul National University Children's Hospital, Seoul 30322, South Korea
[19]Department of Pathology, The Children's Memorial Health Institute, University of Warsaw, 04-730 Warsaw, Poland
[20]Department of Oncology, The Children's Memorial Health Institute, University of Warsaw, 04-730 Warsaw, Poland
[21]Department of Neurosurgery, University of Pittsburgh Medical Center, Pittsburgh, PA 15213, United States of America
[22]Department of Pathology, Centre Hospitalier Universitaire Sainte-Justine, Université de Montréal, Montreal, QC H3T 1C5, Canada

(Affiliations continued on next page)

SUMMARY

Posterior fossa group A (PFA) ependymoma is a lethal brain cancer diagnosed in infants and young children. The lack of driver events in the PFA linear genome led us to search its 3D genome for characteristic features. Here, we reconstructed 3D genomes from diverse childhood tumor types and uncovered a global topology in PFA that is highly reminiscent of stem and progenitor cells in a variety of human tissues. A remarkable feature exclusively present in PFA are type B ultra long-range interactions in PFAs (TULIPs), regions separated by great distances along the linear genome that interact with each other in the 3D nuclear space with surprising strength. TULIPs occur in all PFA samples and recur at predictable genomic coordinates, and their formation is induced by expression of EZHIP. The universality of TULIPs across PFA samples suggests a conservation of molecular principles that could be exploited therapeutically.

INTRODUCTION

Ependymomas (EPNs) are heterogeneous tumors of the central nervous system (CNS) that may occur at multiple anatomical sites, including the supratentorial (STE) and posterior fossa (PF) regions of the brain, and along the spinal cord with site-specific molecular profiles (reviewed in Saleh et al.[1]). Two major molecular subgroups of PF EPN have been defined based on DNA methylation profiles: (a) PF group A (PFA), characterized by the CpG island methylator phenotype (CIMP) and (b) PFB, which lacks the CIMP profile.[2] PFA and PFB EPN are associated with distinct biological and clinical parameters. For instance, PFAs

Please cite this article in press as: Johnston et al., TULIPs decorate the three-dimensional genome of PFA ependymoma, Cell (2024), https://doi.org/10.1016/j.cell.2024.06.023

CellPress
OPEN ACCESS

Cell
Article

Wieslawa Grajkowska,[19] Marta Perek-Polnik,[20] Sameer Agnihotri,[21] Stephen Mack,[12] Benjamin Ellezam,[22] Alex Weil,[23] Jeremy Rich,[24,25] Guillaume Bourque,[6,26] Jennifer A. Chan,[1,2,27] V. Wee Yong,[1,2,9,27,28,29] Mathieu Lupien,[30,31,32] Jiannis Ragoussis,[6,26] Claudia Kleinman,[6,33] Jacek Majewski,[6] Mathieu Blanchette,[10,11] Nada Jabado,[6,13,34,39,*] Michael D. Taylor,[3,4,5,35,36,37,39,*] and Marco Gallo[1,2,9,35,36,37,39,40,*]

[23]Department of Pediatric Neurosurgery, Centre Hospitalier Universitaire Sainte-Justine, Université de Montréal, Montreal, QC H3T 1C5, Canada
[24]University of Pittsburgh Medical Center, Hillman Cancer Center, Pittsburgh, PA 15213, USA
[25]Department of Neurology, University of Pittsburgh Medical Center, Pittsburgh, PA 15213, USA
[26]McGill Genome Centre, Montreal, QC H3A 0G1, Canada
[27]Department of Oncology, Cumming School of Medicine, University of Calgary, Calgary, AB T2N 4N1, Canada
[28]Department of Clinical Neurosciences, Cumming School of Medicine, University of Calgary, Calgary, AB T2N 4N1, Canada
[29]Hotchkiss Brain Institute, Cumming School of Medicine, University of Calgary, Calgary, AB T2N 4N1, Canada
[30]Princess Margaret Cancer Centre, University Health Network, Toronto, ON M5G 1L7, Canada
[31]Department of Medical Biophysics, University of Toronto, Toronto, ON M5G 1L7, Canada
[32]Ontario Institute for Cancer Research, Toronto, ON M5G 0A3, Canada
[33]Lady Davis Research Institute, Jewish General Hospital, Montreal, QC H3T 1E2, Canada
[34]Division of Experimental Medicine, Department of Medicine, McGill University, Montreal, QC H3A 3J1, Canada
[35]Department of Pediatrics, Baylor College of Medicine, Houston, TX 77030, USA
[36]Cancer and Hematology Center, Texas Children's Hospital, Houston, TX 77030, USA
[37]Dan L Duncan Comprehensive Cancer Center, Baylor College of Medicine, Houston, TX 77030, USA
[38]These authors contributed equally
[39]Senior author
[40]Lead contact
*Correspondence: nada.jabado@mcgill.ca (N.J.), michael.taylor@bcm.edu (M.D.T.), marco.gallo@bcm.edu (M.G.)
https://doi.org/10.1016/j.cell.2024.06.023

are mostly diagnosed in infants and young children, whereas PFBs occur mostly in adults. In addition to being CIMP$^+$, PFA tumors display depletion of the histone mark H3K27me3, which is deposited by the Polycomb repressive complex 2 (PRC2) and is usually associated with transcriptional repression.[3] Assessment of H3K27me3 depletion by immunohistochemistry is used as a clinical test to support the diagnosis of PFAs.[4] There are at least two established mechanisms for depletion of H3K27me3 in this tumor type. First, 95% of PFAs overexpress EZHIP/CXorf67,[5] a protein that can interact and inhibit EZH2, the catalytic subunit of PRC2.[6] Second, some rare PFAs harbor mutations in the histone 3 variant H3.3 that result in the substitution of lysine to methionine at position 27 (K27M).[7,8] H3.3K27M has been defined as an oncohistone in pediatric high-grade gliomas (HGGs) and interacts with PRC2 to block the spread of H3K27me3.[9–11]

PFA tumors lack recurrent genetic coding mutations. *EZHIP* is one of the most frequently mutated genes, although it is mutated in only ~10% of cases.[12] The vast majority of PFAs are therefore without clear genetic drivers with malignant transformation potential. The low frequency of recurrent coding mutations is consistent with the extremely low mutation burden in this tumor type and has slowed the development of accurate genetic mouse models and targeted therapies.[2] Consequently, PFA patients are usually treated with radiation—which causes significant developmental sequelae—and no chemotherapy has so far shown sufficient efficacy in clinical trials to warrant standard of care status.[1] PFA EPN is therefore a tumor entity defined by aberrant epigenetic landscapes (CIMP$^+$, depletion of H3K27me3), while being genetically bland and lacking recurrent coding mutations.

The epigenomic profile of a cell is associated with the characteristic architecture of its three-dimensional (3D) genome. Seminal work with Hi-C[13,14] established that the genome is organized along a hierarchy of structures—loops, domains, and compartments—that acquire specific configurations in the 3D nucleus.[15] Loops between non-contiguous genomic regions are visualized at the finer resolution of Hi-C experiments. Loops arise from an extrusion mechanism mediated by the cohesin complex and are frequently but not necessarily anchored by CCCTC-binding factor (CTCF) bound to DNA recognition motifs arranged in convergent orientations along the linear genome.[16] Loops can bring *cis*-regulatory elements in proximity with their target genes and are often co-opted to regulate transcriptional levels. Domains, often referred to as topologically associating domains or TADs, are the second major level of organization of the 3D genome and represent strong interactions among contiguous genomic regions. TADs are often delimited by loop anchors to form loop domains, which can be mediated by dimerization of CTCF. The third level of 3D genome organization is represented by compartments, which can be of two major types: A and B.[15] Type A compartments correspond to genomic regions with open chromatin, active transcription, and more central location within the nucleus. Type B compartments correspond to genomic regions with closed chromatin and repressed or low transcription and tend to be located at the nuclear periphery.[17] Loops, domains, and compartments are 3D genome elements that can ultimately contribute to cell-type-specific transcriptional profiles. Disruption of domains and compartment boundary elements may cause developmental disorders[18] or contribute to oncogenic programs.[19–21] Instances of boundary disruption have been reported in brain cancers. They can be caused by loss of CTCF occupancy at domain boundaries, as reported in IDH1-mutant gliomas,[22] or genetic structural variants spanning boundary elements, as observed in medulloblastoma (MB).[23] However,

Please cite this article in press as: Johnston et al., TULIPs decorate the three-dimensional genome of PFA ependymoma, Cell (2024), https://doi.org/10.1016/j.cell.2024.06.023

CellPress
OPEN ACCESS

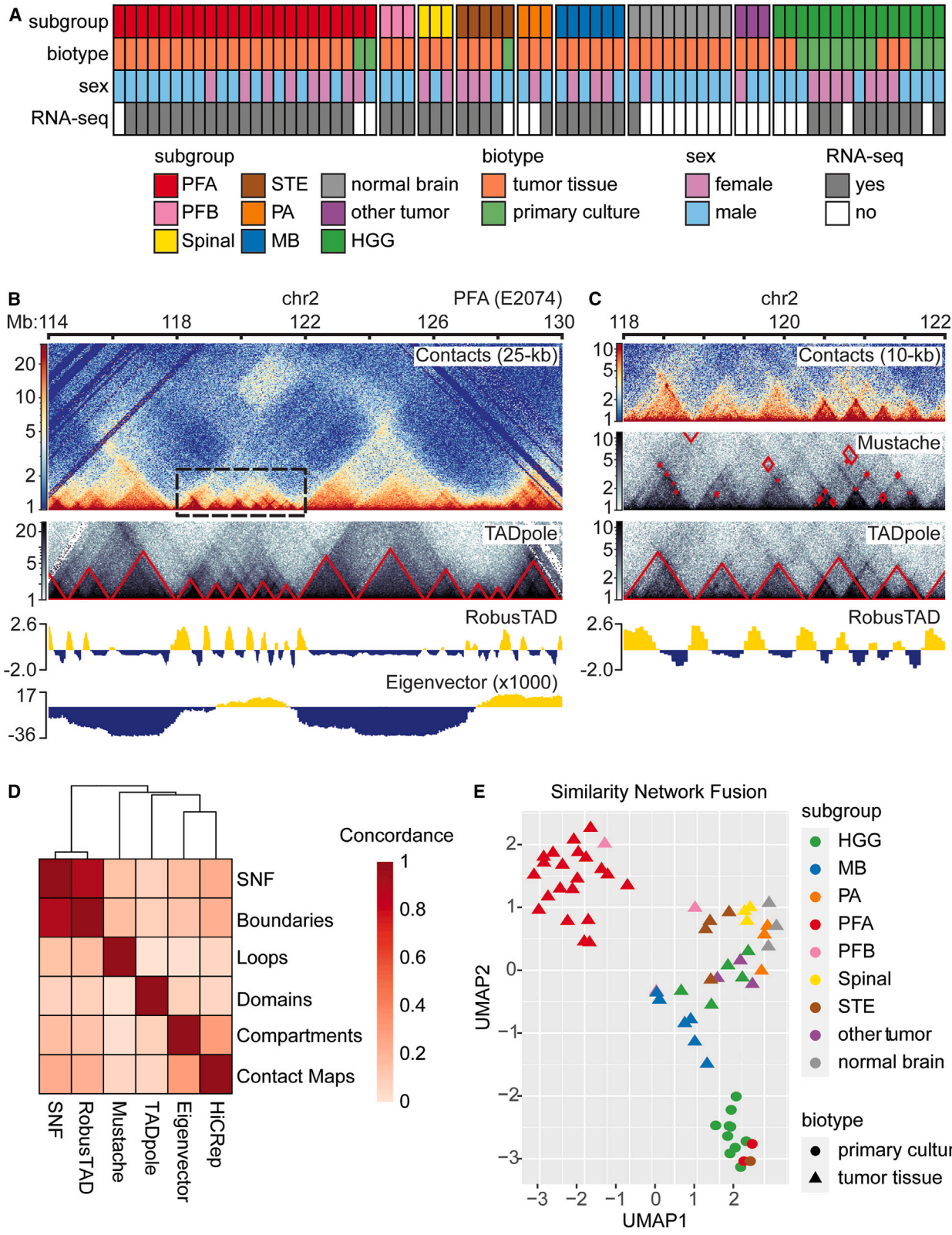

(legend on next page)

Please cite this article in press as: Johnston et al., TULIPs decorate the three-dimensional genome of PFA ependymoma, Cell (2024), https://doi.org/10.1016/j.cell.2024.06.023

studies in brain cancers have mostly relied on targeted chromosome conformation capture approaches to test for disruption of topological domain boundaries. Global approaches that use Hi-C to profile 3D genome architecture have mostly been applied to cell lines or patient-derived cultures.[24] There is currently a dearth of information on the 3D genome of most brain cancers.

In the present study, we have used Hi-C to identify and characterize 3D genome structures that distinguish PFAs from other pathologically and molecularly distinct childhood CNS tumor types and non-neoplastic specimens.

RESULTS

A 3D genome topology atlas of childhood CNS malignancies

We mapped 3D genome topology in childhood CNS tumors using *in situ* Hi-C. We generated Hi-C libraries for 61 tumor samples and 3 non-malignant brain tissues (Figure 1A). In addition, we reanalyzed 6 previously published Hi-C libraries generated from the developing human brain.[25] For patient and sample information, see Table S1. The tumor samples included 51 neoplastic or non-neoplastic tissues and 13 patient-derived primary cultures. Our collection captured distinct CNS tumor types and their main molecular subgroups, including 34 EPNs representing PFA (n = 23), PFB (n = 3), STE (n = 5), and spinal (n = 3) subgroups. We also profiled 15 pediatric HGGs—including histone 3 wild type (WT; n = 4) and histone 3 mutant (n = 11) samples—and 6 MBs representing group 3 (G3; n = 2), group 4 (G4; n = 2), and sonic hedgehog (SHH; n = 2) subgroups. In addition, we generated Hi-C libraries from 9 other tumors, including pilocytic astrocytoma (PA; n = 3). In total, we generated 44 billion reads across all Hi-C libraries, producing 27 billion valid Hi-C contacts. The median resolution of our Hi-C libraries was 6.4 kbp (range: 2.6–87 kbp). To ensure consistency in our downstream analysis, all Hi-C libraries included in our study had contact resolutions <15 kilobases (kb) and at least 90% of all their unique sequencing read pairs resulted in intra-chromosomal contacts separated by >20 kb. For full quality control data, refer to Table S1. The high resolution of our Hi-C maps enabled the analysis of compartments, domains, and loops.

To enable downstream association between 3D genome features and transcription, we generated 52 RNA sequencing (RNA-seq) datasets, 48 of which were paired to Hi-C data in our collection (Figure 1A; Table S1). Overall, our Hi-C and transcriptomic datasets provide an opportunity for integrative studies of a large collection of pediatric CNS tumors.

3D genome topologies distinguish tumor molecular subtypes

Molecular subgrouping of tumor types has historically been based on genetic, transcriptional, and/or DNA methylation profiles. Here, we asked whether 3D genome topology could group CNS tumors based on their diagnoses and molecular subgroups. To maximize robustness, each 3D topology feature was annotated with multiple computational packages whenever possible. We applied HiCCUPS,[15,26] Mustache,[27] and Chromosight[28] to annotate loops; Arrowhead[26] and TADpole[29] to partition the genome into domains; RobusTAD[30] and Insulation Score to calculate boundary scores; and eigenvector decomposition to determine compartments (Figures 1B, 1C, and S1A; Tables S1 and S2). For each feature annotation, as well as the overall Hi-C contact maps, we constructed a distance matrix between the samples (see STAR Methods). Similarity network fusion (SNF)[31] was applied to reduce the diverse signals of the many feature annotations to an integrated singular similarity matrix that allowed clustering of our samples (Figure S1B). To reduce the redundancy of multiple software callers identifying the same feature, we subsequently selected only one caller for each 3D feature type for input into SNF clustering with the reduced representation clustering appearing highly similar to the comprehensive clustering that used multiple callers (Figures 1D and 1E). Application of different callers resulted in different cluster homogeneity; therefore, the degree of similarity between individual callers and the final fused network was assessed (Figures 1D and S1C). Clear segregation between tumor subgroups could be observed across multiple scales for all feature types. Importantly, the final fused network identified three main clusters of samples: one that included all PFA primary tumors; one that included non-PFA primary tumors; and one that represented all patient-derived primary cultures (Figures 1E and S1B). Overall, 3D genome features as measured by Hi-C can distinguish PFAs from other distinct molecular subtypes of pediatric CNS tumors.

PFAs globally exhibit weaker loops than other CNS tumor types and pervasive transcription

Given that our SNF analyses showed that aggregate 3D genome features distinguish PFAs from other pediatric CNS tumors, we sought to identify and define the topological features that were characteristic of this tumor type. First, to probe the polymer properties of chromosomes, we assessed subgroup-specific differences in Hi-C contact probability with increasing genomic separation (Figure 2A). While the rates of monotonic decay were largely consistent across all samples, PFAs exhibited a depletion of short-range interactions. The reduction in contact

Figure 1. 3D genome features segregate pediatric brain tumors by subgroup

(A) Metadata summary of samples profiled by Hi-C and RNA-seq. In total, 61 tumors and 9 non-tumor samples were analyzed.

(B) Example of downstream feature annotation performed on Hi-C contact matrices. Inset dashed rectangle on the left indicates the zoomed region represented in C.

(C) Enlarged view of the region in dashed rectangle in B.

(D) Concordance between annotated 3D genome features and the SNF model. Concordance values closer to one suggest higher similarity. Distance between features was defined as one minus concordance. Rows were clustered based on the Euclidean distance between rows.

(E) UMAP (uniform manifold approximation and projection) projection of SNF affinity between samples.

See also Figure S1 and Tables S1 and S2.

Please cite this article in press as: Johnston et al., TULIPs decorate the three-dimensional genome of PFA ependymoma, Cell (2024), https://doi.org/10.1016/j.cell.2024.06.023

CellPress
OPEN ACCESS

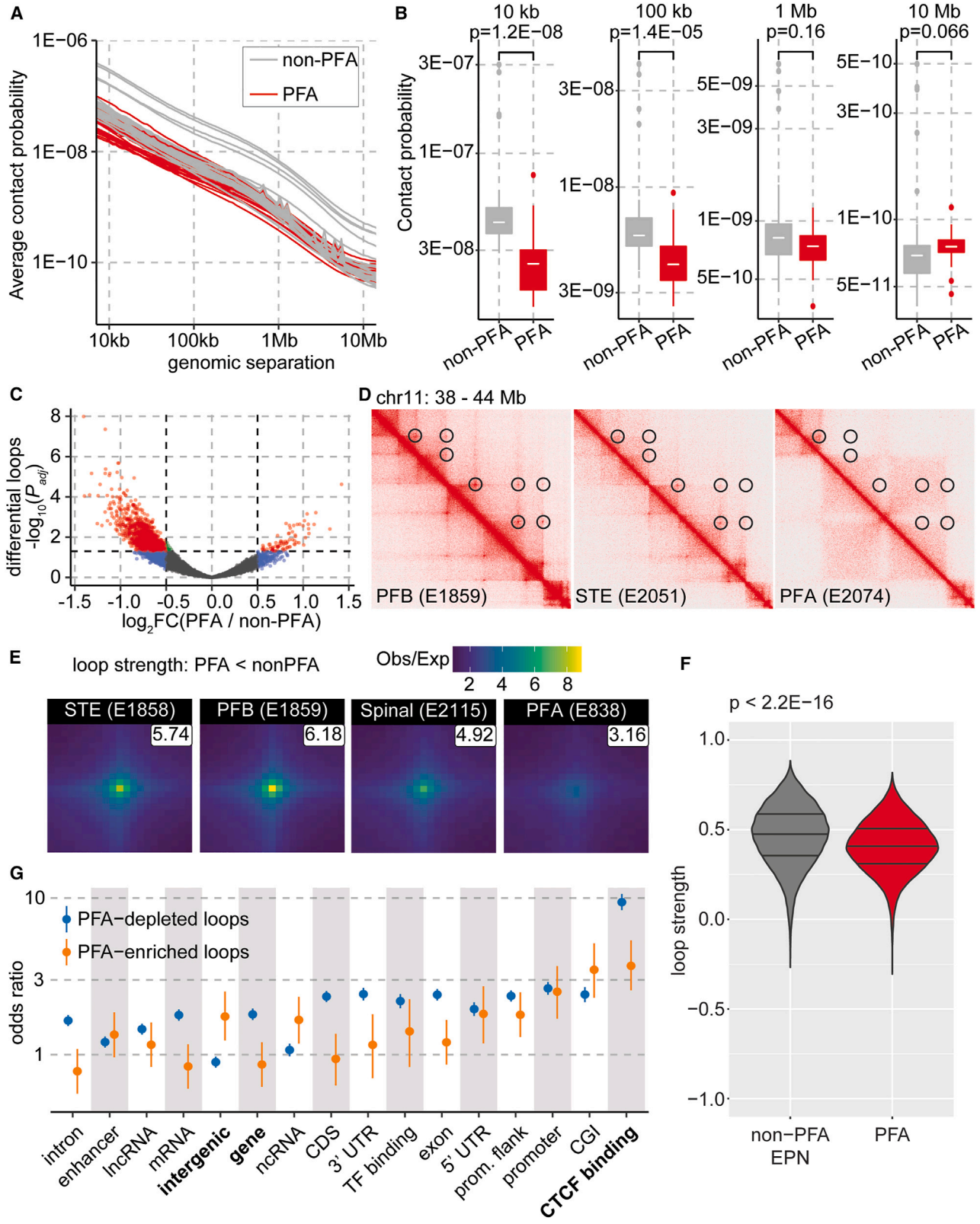

(legend on next page)

Please cite this article in press as: Johnston et al., TULIPs decorate the three-dimensional genome of PFA ependymoma, Cell (2024), https://doi.org/10.1016/j.cell.2024.06.023

probability among PFAs was observed at genomic separations in the sub-100-kb range (10 kb: p = 1.2E-8; 100 kb: p = 1.4E-5), but not at larger separations (1 megabase [Mb]: p = 0.16; 10 Mb: p = 0.066; Figure 2B), findings that are consistent with an attenuation of near-*cis* interactions in the expected size range of most looping interactions. Next, to determine whether the reduced contact probability between regions less than 100 kb apart corresponded to reduced looping interactions in PFAs compared to non-PFA EPNs, we identified chromatin loops across all EPNs with Mustache[27] and subsequently performed differential loop strength analysis with HiCDC+.[32] We found that 1,420 loops were significantly depleted and 82 loops were significantly enriched in PFAs compared to non-PFA EPNs (Figure 2C; Table S3). Loop intensity differences were readily visible on individual Hi-C contact maps (Figure 2D) and aggregate peak analysis (APA) (Figure 2E). A global comparison of loop strength revealed a significantly lower loop strength in PFAs compared to non-PFA EPNs (Wilcoxon rank-sum test $p < 2.2E-16$; Figure 2F), with this difference being independent of loop length (Figure S2A). PFAs therefore exhibit a strong bias toward weaker loop strengths as compared to other EPN subgroups.

Next, we determined the characteristics of the loops that were depleted or enriched in PFA. For both depleted and enriched loops, there was a strong association with CTCF motifs. 86.9% of PFA-depleted anchors overlap CTCF motifs, yielding an odds ratio (OR) of 9.41 (95% confidence interval: 8.37–10.6). Similarly, 72.6% of PFA-enriched anchors overlap CTCF sites (OR 3.69, 95% confidence interval: 2.58–5.37) (Figure 2G). PFA-depleted loops were more strongly associated with mRNA-producing genes, whereas PFA-enriched loops fell within intergenic regions more frequently.

To examine the effects of differential loops on transcription, we performed bulk transcriptome analysis on pediatric tumors, including 48 samples from our Hi-C cohort (Table S4). We performed differential expression analysis between PFA and non-PFA EPN samples (Table S4). Surprisingly, only a small subset of genes associated with differential loops were also differentially expressed in PFAs (48 of 745 genes; Figure S2B). Differential loop strength was not a strong predictor of direction of gene expression.

To test whether the looping patterns we identified in PFA affect transcription of the non-coding space, we performed *de novo* transcriptome assembly with StringTie.[33] With this approach, we identified thousands of intergenic transcripts across all molecular subtypes of pediatric CNS tumors we profiled (Data S1) and quantified their abundance (Table S4). At the two extremes, PFAs had the highest number of intergenic transcripts and HGGs had the lowest (Figure S2C). Some PFA-enriched intergenic transcripts overlapped regions enriched for the activating histone mark H3K27ac[2] and that were identified as super-enhancers (SEs) using ROSE[34,35] (Figure S2D), suggesting that they may be transcribed enhancer RNAs (eRNAs). However, transcription in PFA tumors also occurred at intergenic regions that lacked any inferred SEs or annotated genes (Figure S2D). These results are consistent with the 3D genome architecture of PFA-enabling transcription of intergenic regions.

Large contiguous compartments and strong type B interactions are characteristic of PFA tumors

Hi-C data have revealed that the genome broadly segregates into type A and type B compartments, which largely correspond with euchromatin or heterochromatin, respectively.[14,15] Compartment organization in PFAs was distinct from all other sample types included in this study. Regions of contiguous compartmentalization appear to be larger in PFAs than in non-malignant tissues (Figure 3A) and other tumor types, including other EPN molecular subgroups (Figure 3B). Longer compartment blocks appeared as reduced alternation or "flicker" between compartment types (Figures 3A and 3B). These longer compartment blocks were quantified by assessing the decay of the auto-correlation coefficient for compartment scores,[36] which gauges the average feature size in the compartment score signal (Figure 3C). These results demonstrate that PFA samples (red lines in Figure 3C) have larger compartments than other tumor types (gray lines). To better contextualize these findings, we reprocessed published Hi-C data spanning a diverse range of cell types including cultured cell lines, non-neoplastic primary tissue, and tumor tissues (n = 38, see STAR Methods; Table S5). Interestingly, we found that stem or progenitor cell types—including neural progenitor cells and embryonic stem cells—(yellow lines in Figure 3C) also tend to have larger compartment blocks than more differentiated cell types, including astrocytes of the cerebellum and spinal cord, right temporal lobe, and left temporal lobe tissues (blue lines in Figure 3C). These characteristics showcase a 3D genome topology in PFAs that is reminiscent of undifferentiated cell states.

We next questioned whether the increased size of compartment blocks in PFA could influence the strength with which these compartments interact. Saddle plots[37] displayed stronger B-B interactions in PFAs compared to other tumor types (Figure 3D). This trend was observed for both intra- and inter-chromosomal B-B interactions (Figure 3D).

Figure 2. Short-range looping interactions appear weaker in PFA tumors

(A) Contact probability decay curves comparing PFA to non-PFA tumors.

(B) Differences in contact probability as a function of genomic separation. *P* values calculated using Wilcoxon rank-sum test.

(C) Differential interactions identified by HiCDC+ between PFA and non-PFA EPN for the union set of Mustache-called loops.

(D) Hi-C contact maps comparing loop signals detected from representative examples: PFB (E1859), STE (E2051), and PFA (E2074) tumors. Circles highlight loop signals that are not detected in PFA.

(E) Aggregate peak analysis for representative examples at sites of decreased loop strength in PFA.

(F) Global loop strength comparison between PFA and non-PFA EPN for the union set of Mustache-called loops, quantified by Chromosight. *P* values were calculated using Wilcoxon rank-sum test.

(G) Enrichment of annotated genome features at differential loop loci.

See also Figure S2, Tables S3 and S4, and Data S1.

Please cite this article in press as: Johnston et al., TULIPs decorate the three-dimensional genome of PFA ependymoma, Cell (2024), https://doi.org/10.1016/j.cell.2024.06.023

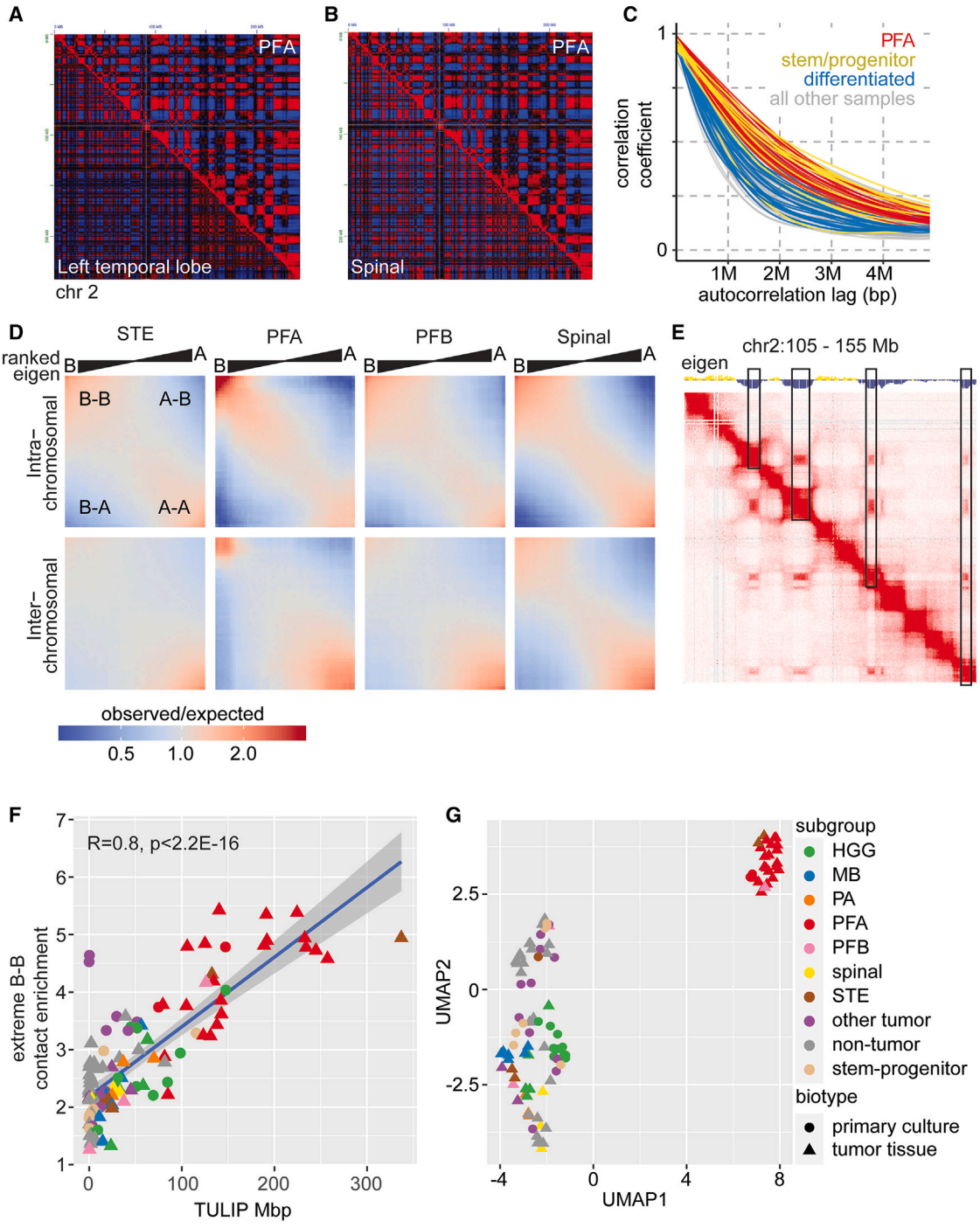

Figure 3. Strict segregation of compartments in PFA

(A) Comparison of Pearson correlation matrices between PFA (E2074) and non-tumor left temporal lobe.

(B) Comparison of Pearson correlation matrices between PFA (E2074) and Spinal ependymoma (E2105).

(C) Autocorrelation decay of compartment scores across tumor and developmental cell types.

(D) Saddle plots comparing contact frequency by compartment status across representative samples for each EPN subgroup: STE (E2051), PFA (E809), PFB (E1859), Spinal (E2061).

(E) Heatmap of Hi-C contacts along a region of chromosome 2. Negative eigen values (blue) identify type B compartments, whereas positive eigen values (yellow) identify type A compartments. Black rectangles highlight portions of each type B compartment that interact with each other over long distances.

(legend continued on next page)

Please cite this article in press as: Johnston et al., TULIPs decorate the three-dimensional genome of PFA ependymoma, Cell (2024), https://doi.org/10.1016/j.cell.2024.06.023

Comparison of the strong homotypic interactions we observed in PFA samples with published Hi-C data (Table S5) revealed *cis* B-B interactions in PFA were significantly stronger than all other non-EPN cell types (Figure S3A). Our analyses therefore support the notion that compartment blocks in PFA are larger and more strictly segregated than in other childhood CNS malignancies, with *cis* B-B interactions being particularly strong.

A subset of type B compartments form unusually strong long-range interactions in PFA tumors

Among the type B interactions we observed in PFA, we identified a subset that were much stronger than others and involved only a portion of the compartment that was demarcated by the most negative eigenvalues (black rectangles in Figure 3E). These regions frequently interact with each other despite being separated by over 10 Mbp along the linear genome. We define these long-distance, strong, and sharp interactions between portions of type B compartments as type B ultra long-range interactions in PFAs (TULIPs).

To determine whether TULIPs are enriched in PFAs compared to other tumors and non-tumor cell types, we designed a computational approach to automate detection of TULIPs based on Hi-C contact matrices in a quantitative, reproducible, and objective fashion (Figures S3B–S3I; Table S5; see STAR Methods). Using this method, the number of TULIP calls was strongly correlated with the extreme B-B contact enrichment (Pearson $p < 2.2E-16$; Figure 3F), with PFA samples uniformly displaying high TULIP signal. Clustering of samples based on the Jaccard distance between TULIP calls sets PFAs clearly apart from the other tumor subgroups, with only 3 non-PFA samples (two STE and one PFB) co-clustering with PFAs (Figure 3G). Given that not all STE and PFB samples displayed TULIPs, future studies with more PFB and STE samples will be required to determine the prevalence of TULIPs in these EPN subtypes.

TULIPs represent highly recurrent 3D topological features in PFA tumors

Pileup analysis of Hi-C contacts between TULIP regions revealed a sharp discontinuity in contact frequency at the boundaries, indicating that TULIPs interact strongly with one another to the exclusion of neighboring genomic DNA (Figure 4A). To further test whether TULIPs indeed represent a special case of type B compartment, we measured homotypic interaction strengths between type A compartments, type B compartments, and TULIPs in our PFA Hi-C datasets. This analysis showed the expected wave-like alternations between strong A-A interactions and B-B interactions along the length of a chromosome (Figure 4B). However, the interactions between TULIP regions in PFA were greater than 5-fold higher than between type B compartment blocks (Figure 4B). These results are consistent with TULIP regions interacting within a subcompartment of the nucleus distinct from typical type B regions.

As Hi-C contact maps are limited to two-dimensional representations of chromatin interactions, we aimed to visualize how TULIPs may impact the organization of the genome in 3D. We derived 3D models of individual chromosomes from our Hi-C data using CSynth.[38] Using a representative PFA tumor, our modeling indicates that recurrent TULIPs on the same chromosome tend to cluster close to each other, as can be seen for chromosome 2 (red regions in Figure 4C). The same regions do not cluster together in PFB (Figure 4D). With a complementary approach, we generated 10,000 whole-nucleus diploid 3D models[39] per sample, assuming comparable contact tendencies across alleles, and confirmed that regions involved in the formation of TULIPs show greater spatial proximity in PFA than corresponding regions in non-PFA EPN tumors (Figure S4A). Quantitatively, mean pairwise distance between TULIP regions was shorter in PFA tumors than in other EPN tumor types for both intra- and inter-chromosomal interactions (two-sided Wilcoxon rank-sum test $p < 2E-16$ for all comparisons; Figures S4B and S4C), although this pattern was much more remarkable for intra-chromosomal interactions.

Finally, we directly tested whether TULIPs aggregate within individual nuclei in PFA clinical specimens. We designed oligo-FISH (fluorescence *in situ* hybridization) probes against three sequential TULIP regions along chromosome 8, and two type A regions interdigitated between the three TULIP regions (Figure 4E). Each targeted region is separated by over 1 Mb in the linear genome (Figure S4D). In PFA tumor resections, the TULIP-targeted FISH probes are observed as individual puncta, separated from the control region probes (Figure 4F). Equivalent imaging of PFB tumors indicate that the TULIP FISH signal is more diffuse in this EPN subtype (Figure 4G), occupying significantly more area in each image (Wilcoxon Rank Sum $p = 2.2E-11$; Figure 4H). Our oligo-FISH experiments using clinical samples validate and confirm Hi-C predictions that TULIPs exist in PFA samples and strongly interact with each other in the 3D nuclear space.

We next assessed the genomic distribution of TULIPs. Strikingly, TULIPs frequently occurred at the same genomic coordinates across PFA samples, including PFA patient-derived cultures (Figure 4I). Recurrent TULIPs, conservatively defined here as TULIPs that occur in at least 20% of PFA samples, occupied 8% of the genome (257 Mbp of 3,088 Mbp, genome reference hg38) with a median TULIP size of 950 kbp (Table S6). PFA primary cultures displayed TULIP calls at the same genomic coordinates as primary tumor specimens (Figure 4I), indicating that these 3D genome features are maintained in patient-derived models. TULIP calls often occurred at pericentromeric and telomeric regions but were also located at other chromosomal regions (Figure 4J). Overall, TULIPs are quantifiable and recurrent 3D genome features in PFA tumors.

Long-read nanopore sequencing of 4 PFA samples in our Hi-C cohort found no mismatched or split-read alignments at the

(F) Extreme B-B contact enrichment vs. TULIP calls. Extreme B-B contact enrichment values represent the mean Obs/Exp value for genomic bins within the 5% most negative compartment eigenvalues, excluding inter-chromosomal contacts and intra-chromosomal contacts separated by <10 Mb. *P* value indicates significance of Pearson correlation. Legend shapes and colors as presented in (C).
(G) UMAP projection of Jaccard distance between TULIP calls for each sample.
See also Figure S3 and Table S5.

Please cite this article in press as: Johnston et al., TULIPs decorate the three-dimensional genome of PFA ependymoma, Cell (2024), https://doi.org/10.1016/j.cell.2024.06.023

CellPress
OPEN ACCESS

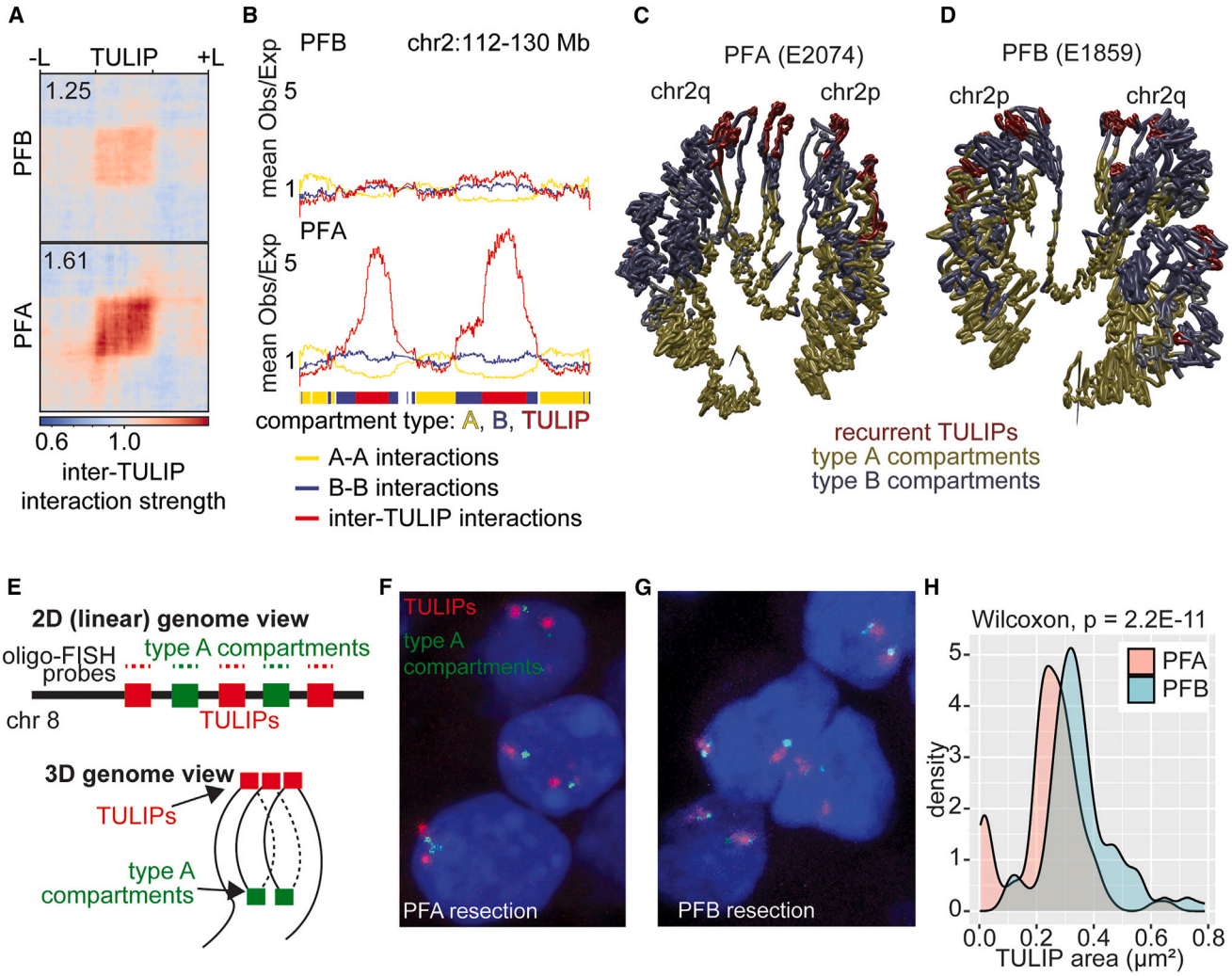

(legend on next page)

Please cite this article in press as: Johnston et al., TULIPs decorate the three-dimensional genome of PFA ependymoma, Cell (2024), https://doi.org/10.1016/j.cell.2024.06.023

boundaries of recurrent TULIPs (data not shown). Furthermore, repeating our analysis of inter-TULIP interaction strength using a Hi-C normalization method that accounts for the presence of copy-number variations (CNVs) in the genome[40] (Figure S4E), we found no evidence that TULIP signals might be a consequence of structural variants.

The local chromatin architecture around TULIPs is distorted in PFA tumors

Having established that TULIPs participate in unusually strong and long-range interactions, we next investigated the relationship between TULIPs and their surrounding topological features. First, we measured loop strength after assigning loops to one of three categories based on loop position relative to recurrent TULIPs (Figure 5A): loops with (1) both anchors outside of TULIPs (loops outside), (2) both anchors within a TULIP (loops inside), or (3) one of the two anchors in a TULIP (loops in/out). In/out loops were significantly weaker than loops fully inside TULIPs (Wilcoxon rank-sum test p = 1.9E-2) or loops that were completely anchored outside of TULIPs (Wilcoxon rank-sum test p = 2.5E-9; Figure 5B), further contributing to the notion that TULIPs are discrete domains insulated from neighboring regions. However, independently of position with respect to TULIPs, all three categories of loops were weaker in PFAs than in non-PFA EPNs (loops outside, Figure S5A p < 2.2E-16; in/out loops, Figure S5B, p = 2.0E-11; or fully anchored inside TULIPs, Figure 5C, p = 2.5E-14 by Wilcoxon rank-sum test). This is consistent with TULIPs being depleted of interactions with adjacent non-TULIP regions (Figures 5D–5F), further supporting the hypothesis that these PFA-specific 3D structures are strongly insulated from the rest of the genome.

We also noticed that some TULIP-flanking regions in type A compartments displayed elevated interaction frequency with each other, albeit considerably weaker than the interactions among TULIPs themselves (Figures 5G–5I). We therefore asked how the presence of TULIPs in the PFA genome might influence overall compartmentalization status. We applied CALDER[41] to our Hi-C data to assign genomic bins along the spectrum of compartmentalization status ranging from most open (A.1.1) to most closed (B.2.2) and subsequently compared the genome compartmentalization status for each bin. In a pairwise comparison between a PFA and a PFB, we observed that 71% of genomic bins had unchanged compartment status, predominately in A.1.1 or B.2.2 (Figure S5C). Surprisingly, the bins that did exhibit altered compartmentalization status tended to be more open in PFAs when compared to PFBs (Figure S5C), whereas comparison between pairs of PFA samples did not show a similar bias toward open compartmentalization status (Figure S5D). To extend this analysis to include all samples and to compare between tumor subgroups, we derived the consensus compartment status (mode average) for each subgroup. Comparing the PFA consensus to the PFB consensus compartmentalization, we observe that the number of bins transitioning from B to A is three times greater than the number transitioning from A to B (Figure 5J). By comparing each sample individually against the non-tumor brain consensus compartmentalization, PFA samples exhibited a significant bias toward open compartmentalization status while PFB, STE, or spinal EPN tumors did not (Figure 5K, two-sided t test with H_0: mu = 0, H_1: mu $\neq$ 0, p = 5.6E-10). Furthermore, pairwise comparisons between PFA samples and consensus compartmentalization status for each tumor subgroup showed a consistent and significant bias toward open compartmentalization in PFA (Figure S5E, two-sided t test with H_0: mu = 0, H_1: mu $\neq$ 0, $p \leq$ 2.6E-08 for all comparisons). Finally, we asked whether these compartment transitions impacted transcription and found that transcription was elevated among the bins that had undergone type B-to-A transition, consistent with higher transcription in regions with more open chromatin (Figure 5L). Therefore, compartmentalization of the 3D genome of PFA exhibits two extreme behaviors, with TULIPs representing strongly compacted regions and other regions of the genome acquiring globally more relaxed and transcriptionally active conformations.

TULIP interactions depend on high levels of the repressive chromatin mark H3K9me3

We next sought to describe the chromatin landscape of TULIPs. We performed chromatin immunoprecipitation with sequencing (ChIP-seq) for the repressive histone marks H3K27me3 and H3K9me3 on ten PFA samples where sufficient primary tissue remained available for analysis. Broad regions of high H3K9me3 signal showed considerable overlap with recurrent TULIP loci (Figure 6A). In fact, strong ChIP signal for H3K9me3 was highly predictive for the presence of TULIPs at any given genome region (Figures 6A and S6A), suggesting that TULIPs may form at regions enriched for H3K9me3. Regions of TULIPs and broad H3K9me3 peaks occurred closer together than expected by chance (Figure 6B; p = 3.2E-8) and exhibited significant overlap

Figure 4. PFAs are characterized by TULIPs, 3D structures with high interaction strength across long distances

(A) Aggregate inter-TULIP interaction strength for representative PFA (E2074) and PFB (E1859). Regions have been rescaled such that each TULIP of length L is flanked by a genomic region of equal size upstream (-L) and downstream (+L) of the TULIP.

(B) Mean observed/expected value for each 50-kbp bin, separated by interacting compartment types, excluding signal from contacts between regions that are <10 Mbp apart. PFA: E2074; PFB: E1859.

(C) CSynth model comparing TULIP distribution in 3D space for PFA (E2074).

(D) CSynth model comparing TULIP distribution in 3D space for PFB (E1859).

(E) Schematic of oligo-FISH probe design. TULIP probes in red. Type A compartment probes in green. Diagram is not drawn to scale.

(F) Oligo-FISH signal from PFA surgical resection.

(G) Oligo-FISH signal from PFB surgical resection.

(H) Comparison of area covered by TULIPs in PFA against corresponding genomic regions in PFB. *P* values were calculated using Wilcoxon rank-sum test.

(I) Genomic coordinates of TULIPs across multiple PFA samples. Displayed region is chromosome 2.

(J) Genomic coordinates of recurrent TULIP calls.

See also Figure S4 and Table S6.

Please cite this article in press as: Johnston et al., TULIPs decorate the three-dimensional genome of PFA ependymoma, Cell (2024), https://doi.org/10.1016/j.cell.2024.06.023

CellPress
OPEN ACCESS

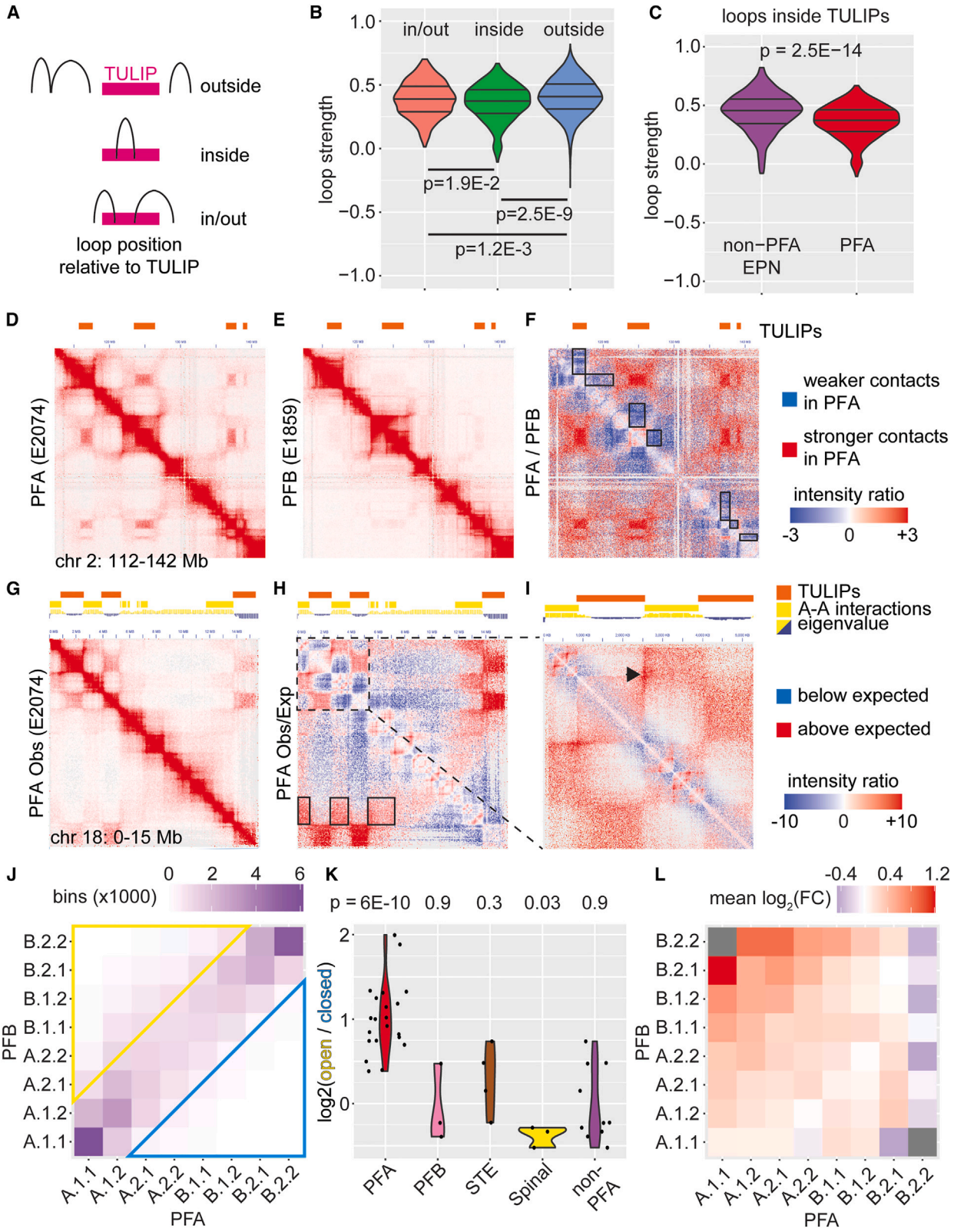

(legend on next page)

Please cite this article in press as: Johnston et al., TULIPs decorate the three-dimensional genome of PFA ependymoma, Cell (2024), https://doi.org/10.1016/j.cell.2024.06.023

(Fisher's exact $p < 1.5E-66$). In contrast, H3K27me3, which is known to be largely depleted in PFA, did not show consistent enrichment within TULIPs (Figure S6B). Considering the strong enrichment of H3K9me3 within recurrent TULIPs, we performed H3K9me3 immunofluorescence to see if the sub-nuclear localization of this histone mark is consistent with the predicted organization of TULIPs within cell nuclei. In PFA, H3K9me3 formed large foci throughout the nucleus (Figure 6C) in contrast to PFB EPN, where H3K9me3 was more distributed throughout the nuclei (Figure 6D). These results are congruent with the notion that H3K9me3$^+$ TULIPs aggregate in the 3D space of the PFA nucleus.

H3K9me3$^+$ heterochromatin is often associated with HP1-family proteins, which link heterochromatin to the nuclear membrane. Given the unusual localization of H3K9me3$^+$ TULIPs in PFA, we tested whether TULIPs are associated with HP1 proteins in PFA cells by immunofluorescence. Overall, HP1 proteins localized to the large foci of H3K9me3, with HP1γ showing the strongest colocalization and HP1α being more diffuse throughout the nucleus (Figures 6E and S6C). We next embarked on analyses to reconstruct the genomic and epigenomic context of TULIPs. First, we compared TULIPs with other genomic annotations associated with chromatin activity. Annotations for protein coding regions (GENCODE v34 annotations) and H3K27ac peaks in PFA[42] were both depleted within TULIPs (Figures S6D and S6E). Overall, these data support a heterochromatic identity for TULIPs.

Among all repetitive elements, young ERV (endogenous retrovirus) family members were strongly enriched in TULIPs, particularly ERV1, ERVL, and ERVK elements (Figure S6F), which tend to be enriched in heterochromatic regions of the genome.[43] Altogether, these results suggest that TULIPs are heterochromatic regions distinct from type B compartments.

Considering the H3K9me3 ChIP signal associated with TULIPs (Figures 6A and 6B), we asked whether enrichment of H3K9me3 is functionally important for the maintenance of TULIPs. For our functional studies, we used inhibitors of G9a/GLP, which are responsible for the deposition of H3K9me2, and chaetocin, which inhibits SUV39H1 and SUV39H2, two enzymes responsible for the deposition of H3K9me3. Treatment of PFA patient-derived cultures with the G9a/GLP inhibitor UNC0642 resulted in an increased number of detectable individual foci (Figures 6F and S6G) and a larger radius per puncta detected (Figure 6G) in oligo-FISH assays described above to detect TULIPs. These results support the notion that loss of H3K9 methylation leads to "melting," or weaker interactions, among TULIPs. Two distinct G9a/GLP inhibitors (UNC0642 and A366) were also effective at impairing cell viability of four patient-derived PFA primary cultures, with IC_{50} concentrations generally <1 μM (Figure 6H). Collectively our data indicate that aggregation of TULIPs in the 3D nuclear space of PFA cells depends on the maintenance of robust levels of H3K9me3 and that TULIP interactions are important for PFA cell viability.

EZHIP promotes TULIP formation

Given that EZHIP is expressed in most PFA tumors, we tested the hypothesis that this protein might be involved in TULIP formation. We stably expressed EZHIP in primary cultures enriched for human neural progenitor cells (hNPCs). Assessment of protein levels by western blot confirmed that expression of EZHIP in these cells (EZHIP OE [overexpression]) was robust, with no or minimal expression of EZHIP in hNPCs transfected with empty control vector (Figure 7A). EZHIP overexpression resulted in reduced H3K27me3 levels (Figure S7A) and increased H3K27ac (Figure S7B), recapitulating the known physiological functions of this protein.

We then investigated whether EZHIP expression alters functional properties of hNPCs. Cell proliferation—assessed by incorporation of the thymidine analog EdU (5-ethynyl-2'-deoxyuridine; see STAR Methods)—showed that EZHIP OE cells had an ~2-fold increase in the fraction of EdU$^+$ cells compared to control cells (Figures 7B and 7C). However, EZHIP expression did not affect self-renewal of hNPCs, assessed with *in vitro* limiting dilution assays (data not shown). The positive effect of EZHIP on hNPC proliferation supports its role in the pathophysiology of PFA EPN.

Next, we asked whether EZHIP expression affects chromatin architecture. Given that TULIPs are exquisitely enriched with H3K9me3, we focused on this histone mark for our experiments. Using immunofluorescence, we found that EZHIP OE cells formed large foci of H3K9me3$^+$ chromatin located in central positions of the nucleus and that were highly reminiscent of TULIPs (Figure 7C), in marked distinction from control cells (Figure 7E). These results were highly reproducible in different hNPC EZHIP OE models we generated (Figures S7C and S7D). To further test the functional role of EZHIP in restructuring

Figure 5. TULIPs distort local 3D topology

(A) Schematic of different potential loop positions relative to TULIPs.

(B) Comparison of looping interactions within PFAs, separated by their position relative to TULIPs. Distributions were compared using two-sided t tests. Horizontal lines indicate 25th, 50th, and 75th percentiles.

(C) Comparison of interactions of loops inside TULIPs in PFA and non-PFA ependymoma. Distributions were compared using two-sided t-tests. Horizontal lines indicate 25th, 50th, and 75th percentiles.

(D–F) Hi-C contact maps contrasting interactions between adjacent domains in (D) PFA and (E) PFB. Black rectangles in (F) highlight TULIP-adjacent contacts.

(G–I) Hi-C contact maps focusing on the interaction patterns of type A compartments adjacent TULIPs in PFA. The heatmaps display (G) observed contacts, (H) the ratio of observed to expected contacts and (I) an enlargement of the square outlined with dashed lines in (H).

(J) Comparison of consensus compartment status between PFA and PFB using CALDER. For PFA compared to PFB, yellow triangle = type B-to-A transition; blue triangle = type A-to-B transition.

(K) Summary of pairwise comparisons between individual samples and non-tumor consensus compartmentalization. Two-sided t test with H_0: mean = 0 and H_1: mean $\neq$ 0.

(L) Heatmap displaying the average $\log_2$ fold change in RNA-seq comparing PFA to non-PFA EPN within each of the compartment transitions displayed in (J). See also Figure S5.

Please cite this article in press as: Johnston et al., TULIPs decorate the three-dimensional genome of PFA ependymoma, Cell (2024), https://doi.org/10.1016/j.cell.2024.06.023

CellPress
OPEN ACCESS

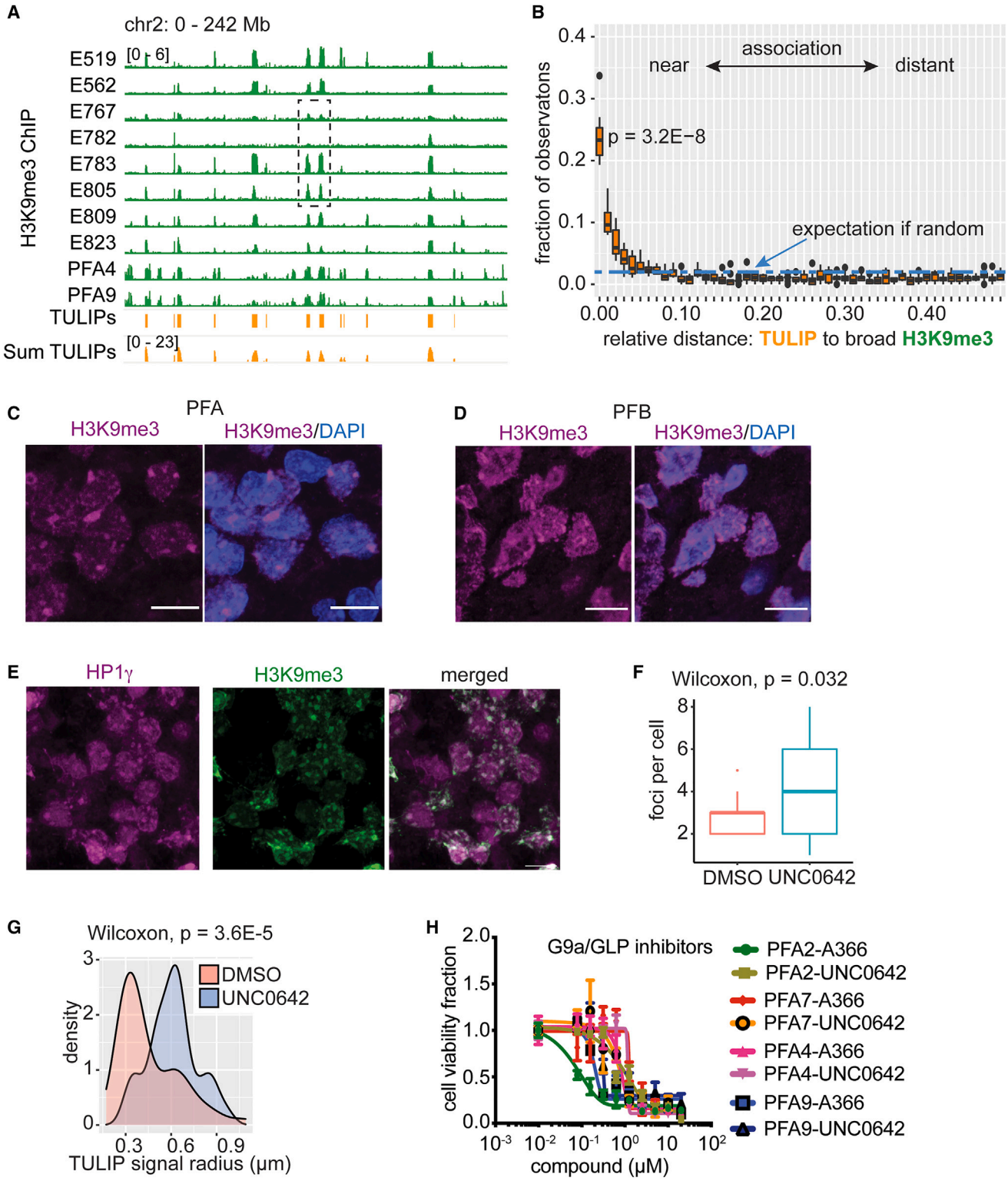

Figure 6. TULIPs are associated with features of heterochromatin

(A) Genome tracks for H3K9me3 ChIP (green) and recurrent TULIPs (orange). Inset dashed line corresponds to genome range in Figure S6B.

(B) Relative distance between TULIP calls and broad regions of H3K9me3. Dashed cyan line indicates expected distribution for random association. *p*-value calculated using one-sided t test for the fraction of observations at relative distance = 0 vs. the expected value of 0.02.

(legend continued on next page)

Please cite this article in press as: Johnston et al., TULIPs decorate the three-dimensional genome of PFA ependymoma, Cell (2024), https://doi.org/10.1016/j.cell.2024.06.023

heterochromatin, we performed transient expression of either WT or a mutant form of EZHIP with an R405E amino acid substitution, which affects the conserved peptide of EZHIP and blocks its direct inhibition of PRC2.[5] As expected, transient expression of EZHIP resulted in the formation of large and intense foci of H3K9me3, whereas the H3K9me3$^+$ foci were smaller and less intense in cells expressing EZHIP R405E (Figures 7F–7H and S7E). EZHIP expression in hNPCs therefore leads to restructuring of H3K9me3$^+$ chromatin to form large foci located in central regions of the nuclei that are highly reminiscent of TULIPs in PFA cells. Similar to TULIPs, the large H3K9me3$^+$ foci in EZHIP OE cells colocalize with HP1γ (Figure S7F). Consistent with established the role of HP1 proteins in maintaining heterochromatin regions in liquid condensates, treating EZHIP OE hNPCs with 1,6-hexanediol destabilized the H3K9me3$^+$ foci in a concentration-dependent fashion (Figure S7G).

The formation of large foci of H3K9me3$^+$ chromatin EZHIP OE cells occurred without significant changes in the global levels of H3K9me3 (Figure S7H). These results, together with the enrichment of H3K9me3 at TULIPs in PFA cells (Figures 6A, 6B, and S6A), suggest that TULIPs might arise from large-scale reorganization of H3K9me3. Altogether, our experiments suggest that TULIPs arise through EZHIP-mediated global reorganization of H3K9me3 and chromatin in the PFA nucleus.

DISCUSSION

Dysregulation of 3D genome architecture has not yet been extensively explored in the context of cancer and especially childhood malignancies. Our approach of generating Hi-C datasets from a large cohort of samples spanning multiple tumor types enabled the identification of recurrent, PFA-specific 3D genome features and allowed their contextualization with other malignancies and with non-malignant tissues.

Our Hi-C studies revealed that PFA EPN is characterized by private 3D genome architecture. PFA stood out among pediatric brain malignancies for possessing 3D structures that we defined as TULIPs, special cases of type B compartmentalization that occur at recurrent positions across PFAs. Given the paucity of recurrent genetic coding events in PFA, the identification of TULIPs as recurrent 3D genome features in this cancer type is particularly meaningful. Our data suggest that TULIPs are defining characteristics of PFA.

The molecular mechanism that leads to formation of TULIPs was an important question we aimed to address. Our data indicate that EZHIP expression is at least partially responsible for their formation. Although the exact molecular events linking EZHIP and TULIP formation need to be further investigated, the data we generated hint at a potential mechanism. EZHIP expression leads to global loss of H3K27me3, as previously established.[6,11] This leaves large blocks of constitutive heterochromatin marked by H3K9me3 to become more insulated from the rest of the genome, and to interact with each other more strongly, leading to the formation of TULIPs. This model is consistent with heterochromatin having a strong tendency to self-interaction, which is the fundamental basis for the organizational principles of chromatin in the 3D nuclear space.[44] TULIPs might therefore be primed to strong interactions among each other because of their heterochromatic nature, and because their interactions are not "diluted" by interactions among neighboring regions of facultative heterochromatin marked by H3K27me3. This causal link could explain why both EZHIP and TULIPs are virtually universal molecular features of PFA EPN. However, EZHIP might also play a more direct role in the establishment of TULIPs because H3K27me3 depletion may not be sufficient for TULIP formation, given that histone-3-mutant HGG samples are also depleted of this histone mark[9,11] but lack TULIPs. Alternatively, the function of EZHIP in initiating TULIPs might be enabled by a specific epigenetic state of the cell of origin of PFA EPN. Future work will need to determine whether EZHIP expression and TULIP formation are features of the PFA cell of origin or if these characteristics are acquired at later stages of the tumorigenic process.

The picture that emerges from our studies indicates that the 3D genome of PFA tumors is an ensemble of extremes: regions that are normally compacted become extremely compacted (TULIPs), while regions outside of TULIPs, including other type B compartments, appear more relaxed overall. Chromatin relaxation in PFA was consistent with significant depletion of loops and pervasive transcription, suggesting dysregulation of transcriptional control. We therefore propose that TULIPs are the last bastions of heterochromatin in a genome that is globally more relaxed and transcriptionally active (Figure 7G).

The global relaxation of chromatin and the compartment organization (Figures 3A–3C) we observed in PFA are reminiscent of what has been reported in embryonic stem cells[45] and in undifferentiated malignant cells in adult glioblastoma.[46] We therefore speculate that the 3D genome of PFA is shaped to maximize the stemness characteristics of these malignant cells to propagate the tumor.

TULIPs are often surrounded by type A compartments that strongly interact with each other. We think it is possible that TULIPs may act in some circumstances as scaffolds for

(C) Immunofluorescence for H3K9me3 (purple) in a PFA surgical specimen. Scale bar: 50 μm
(D) Immunofluorescence for H3K9me3 (purple) in a PFB surgical specimen. Scale bar: 50 μm
(E) Immunofluorescence for HP1g (purple) and H3K9me3 (green) in a PFA surgical specimen. Scale bar: 50 μm
(F) Quantification of oligo-FISH foci per cell. Oligo-FISH probes were designed to detect three TULIPs located on chromosome 8, as described in the text. *p*-value was calculated with the Wilcoxon test.
(G) Quantification of TULIP signal radius determined with oligo-FISH probes imaged with confocal microscopy. PFA cells were treated with DMSO (control) or with UNC0642. *P* value was calculated with the Wilcoxon test.
(H) Dose-response curve for two G9a/GLP inhibitors (A366 and UNC6042) in four PFA patient-derived cultures (PFA2, PFA7, PFA4, and PFA9). Error bars represent standard deviation.
See also Figure S6.

Please cite this article in press as: Johnston et al., TULIPs decorate the three-dimensional genome of PFA ependymoma, Cell (2024), https://doi.org/10.1016/j.cell.2024.06.023

CellPress
OPEN ACCESS

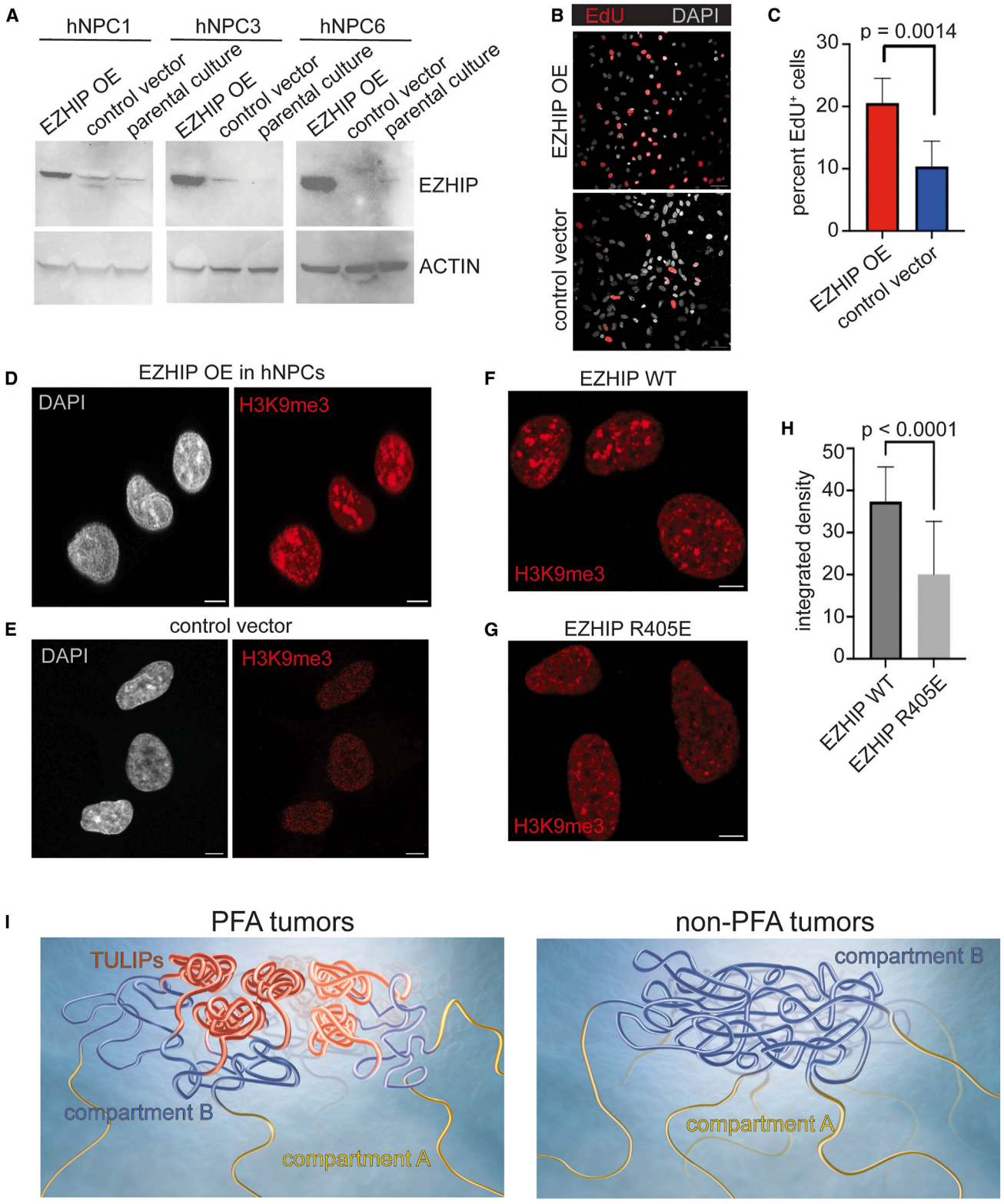

Figure 7. TULIP aggregation is dependent upon the H3K9me3 histone mark

(A) EZHIP protein levels in hNPC overexpression models were assessed by western blot.

(B) Immunocytochemistry for EdU in EZHIP overexpression and control cells. Scale bar: 20 μm

(legend continued on next page)

hairpin-like strong type A compartment interactions, which might be required to bring actively transcribed regions together, as previously reported in primary immune cells.[47] This compartment organization would be an efficient way of orchestrating local regions of active transcription and potentially segregate active and inactive regulatory regions in 3D space.

Surprisingly, we could find no evidence that TULIPs directly participate in regulating gene expression. Although it might appear paradoxical that an inherently epigenetic structure like TULIPs does not affect gene transcription levels, our finding is in line with recent papers that clearly demonstrated a lack of direct correlation between 3D genome topology and gene expression. For instance, acute depletion of cohesin[48] or CTCF[49] lead to erasing TADs or loop domains, and yet only a few genes were differentially expressed. The 3D genome has roles other than gene regulation, including modulation of DNA repair and mutational rates[50] and control of DNA replication timing (reviewed in Flyamer et al.[51]).

In conclusion, our comparative 3D genome studies highlighted previously unknown features of PFAs, including TULIPs and a generalized reorganization of genome topology. Our findings strengthen the hypothesis that PFA is a tumor type exquisitely shaped by epigenomic forces.

Limitations of the study

Ideally, the functional significance of TULIPs in PFA would be assessed through genome engineering approaches that delete multiple TULIPs at once. However, the average size of TULIPs is approximately 1 Mb, making the removal of multiple TULIPs in the same cell prohibitively difficult with current techniques. This problem is exacerbated by the difficulty of working with the few PFA patient-derived models that are currently available. However, the exquisite enrichment of H3K9me3 at TULIPs provided an opportunity to target these regions genome-wide with epidrugs and assess their functional significance. Inhibiting H3K9 methylation "melted" TULIPs and reduced PFA cell viability at low concentrations *in vitro*. These functional studies therefore established that TULIPs are functionally important for PFA cells. Although the compounds we used are not clinical grade, we envision the development of future epidrugs capable of inhibiting H3K9 methylation in clinical settings.

STAR★METHODS

Detailed methods are provided in the online version of this paper and include the following:

- KEY RESOURCES TABLE
- RESOURCE AVAILABILITY
  - Lead contact
  - Materials availability
  - Data and code availability
- EXPERIMENTAL MODEL AND STUDY PARTICIPANT DETAILS
  - Human samples
  - Primary cell cultures
- METHOD DETAILS
  - Hi-C library preparation
  - Hi-C data analysis
  - Transcriptome analysis
  - Differentially methylated regions
  - Aggregation of DNA methylation
  - Super-enhancers (SEs)
  - ChIP-seq
  - Oxford nanopore long-read sequencing
  - OncoPrint
  - Immunohistochemistry of primary tumors
  - Immunocytochemistry
  - Western blot
  - Proliferation EdU assay
  - 1,6-Hexanediol treatment
  - Fluorescence *in situ* hybridization
  - Chemical inhibitors
  - Generation of EZHIP overexpression cultures
  - Transfection for wild type and mutant EZHIP overexpression experiments
- QUANTIFICATION AND STATISTICAL ANALYSIS

SUPPLEMENTAL INFORMATION

Supplemental information can be found online at https://doi.org/10.1016/j.cell.2024.06.023.

ACKNOWLEDGMENTS

This work was supported by a Large-Scale Applied Research Project grant from Génome Québec, Genome Canada, the Government of Canada and Ministère de l'Économie et de l'Innovation du Québec, with the support of the Ontario Research Foundation through funding provided by the Government of Ontario to N. Jabado, M.D.T., J.M., M.B., C.K., J. Ragoussis, M.L., and G.B.; by the Brain Canada Foundation through the Canada Brain Research Fund, with the financial support of Health Canada and the Azrieli Foundation through an Azrieli Future Leader in Canadian Brain Research grant to M. Gallo; Canadian Institutes of Health Research (CIHR) project grants (PJT-156278 and PJT-173475) to M. Gallo; a CIHR postdoctoral fellowship to M.J.J.; a Canada Research Chair to M. Gallo.

AUTHOR CONTRIBUTIONS

M. Gallo, M.B., M.D.T., and N. Jabado designed the study. M.J.J., J.J.Y.L., B.H., A.N., A.B., E.H., S.P., H.C., S.K., C.C.L.C., S.J., P. Balin, V.F., M.Z., A.M., X.C., Y.Z., S.V., and P. Billon executed the experimental activities. J.M., C.K., J. Ragoussis, J. Rich, M.L., J.A.C., G.B., S.M., B.E., S.A., M.P.-P., W.G., J.Y.L., K.-C.W., S.-K.K., B.-K.C., Y.S.R., T.P., P.H., M. Garami,

(C) Quantification of the fraction of cells positive for EdU. *P* value was calculated with a t test. Error bars represent standard deviation.
(D) Immunofluorescence for H3K9me3 in EZHIP overexpression hNPCs. Scale bar: 5 μm
(E) Immunofluorescence for H3K9me3 in control hNPCs. Scale bar: 5 μm
(F) Immunofluorescence for H3K9me3 in hNPCs transiently transfected with a plasmid for expression of wild-type EZHIP. Scale bar: 20 μm
(G) Immunofluorescence for H3K9me3 in hNPCs transiently transfected with a control plasmid for expression of a mutant for of EZHIP. Scale bar: 20 μm
(H) Integrated density of H3K9me3 foci was computed for hNPCs expressing wild-type or mutant EZHIP. *P* value was computed by t test. Error bars represent standard deviation.
(I) Diagram summarizing the main differences between the 3D genome of PFA tumors compared to other tumor types, with a focus on the presence of TULIPs in PFA.
See also Figure S7.

E.M.T., C.G., A.N.R., C.D., and N. Juretic had roles in supervising various aspects of the project and in aiding sample and data collection. M. Gallo, M.B., M.D.T., N. Jabado, M.L., M.J.J., J.J.Y.L., A.B., B.H., and H.C. contributed to writing this paper.

DECLARATION OF INTERESTS

The authors declare no competing interests.

Received: August 27, 2021
Revised: May 26, 2022
Accepted: June 18, 2024
Published: July 9, 2024

REFERENCES

1. Saleh, A.H., Samuel, N., Juraschka, K., Saleh, M.H., Taylor, M.D., and Fehlings, M.G. (2022). The biology of ependymomas and emerging novel therapies. Nat. Rev. Cancer *22*, 208–222. https://doi.org/10.1038/s41568-021-00433-2.
2. Mack, S.C., Witt, H., Piro, R.M., Gu, L., Zuyderduyn, S., Stütz, A.M., Wang, X., Gallo, M., Garzia, L., Zayne, K., et al. (2014). Epigenomic alterations define lethal CIMP-positive ependymomas of infancy. Nature *506*, 445–450. https://doi.org/10.1038/nature13108.
3. Bayliss, J., Mukherjee, P., Lu, C., Jain, S.U., Chung, C., Martinez, D., Sabari, B., Margol, A.S., Panwalkar, P., Parolia, A., et al. (2016). Lowered H3K27me3 and DNA hypomethylation define poorly prognostic pediatric posterior fossa ependymomas. Sci. Transl. Med. *8*, 366ra161. https://doi.org/10.1126/scitranslmed.aah6904.
4. Panwalkar, P., Clark, J., Ramaswamy, V., Hawes, D., Yang, F., Dunham, C., Yip, S., Hukin, J., Sun, Y., Schipper, M.J., et al. (2017). Immunohistochemical analysis of H3K27me3 demonstrates global reduction in group-A childhood posterior fossa ependymoma and is a powerful predictor of outcome. Acta Neuropathol. *134*, 705–714. https://doi.org/10.1007/s00401-017-1752-4.
5. Jain, S.U., Do, T.J., Lund, P.J., Rashoff, A.Q., Diehl, K.L., Cieslik, M., Bajic, A., Juretic, N., Deshmukh, S., Venneti, S., et al. (2019). PFA ependymoma-associated protein EZHIP inhibits PRC2 activity through a H3 K27M-like mechanism. Nat. Commun. *10*, 2146. https://doi.org/10.1038/s41467-019-09981-6.
6. Jain, S.U., Rashoff, A.Q., Krabbenhoft, S.D., Hoelper, D., Do, T.J., Gibson, T.J., Lundgren, S.M., Bondra, E.R., Deshmukh, S., Harutyunyan, A.S., et al. (2020). H3 K27M and EZHIP Impede H3K27-Methylation Spreading by Inhibiting Allosterically Stimulated PRC2. Mol. Cell *80*, 726–735.e7. https://doi.org/10.1016/j.molcel.2020.09.028.
7. Ryall, S., Guzman, M., Elbabaa, S.K., Luu, B., Mack, S.C., Zapotocky, M., Taylor, M.D., Hawkins, C., and Ramaswamy, V. (2017). H3 K27M mutations are extremely rare in posterior fossa group A ependymoma. Childs Nerv. Syst. *33*, 1047–1051. https://doi.org/10.1007/s00381-017-3481-3.
8. Gessi, M., Capper, D., Sahm, F., Huang, K., von Deimling, A., Tippelt, S., Fleischhack, G., Scherbaum, D., Alfer, J., Juhnke, B.-O., et al. (2016). Evidence of H3 K27M mutations in posterior fossa ependymomas. Acta Neuropathol. *132*, 635–637. https://doi.org/10.1007/s00401-016-1608-3.
9. Schwartzentruber, J., Korshunov, A., Liu, X.Y., Jones, D.T.W., Pfaff, E., Jacob, K., Sturm, D., Fontebasso, A.M., Quang, D.A.K., Tönjes, M., et al. (2012). Driver mutations in histone H3.3 and chromatin remodelling genes in paediatric glioblastoma. Nature *482*, 226–231. https://doi.org/10.1038/nature10833.
10. Sturm, D., Witt, H., Hovestadt, V., Khuong-Quang, D.A., Jones, D.T.W., Konermann, C., Pfaff, E., Tönjes, M., Sill, M., Bender, S., et al. (2012). Hotspot Mutations in H3F3A and IDH1 Define Distinct Epigenetic and Biological Subgroups of Glioblastoma. Cancer Cell *22*, 425–437. https://doi.org/10.1016/j.ccr.2012.08.024.
11. Harutyunyan, A.S., Krug, B., Chen, H., Papillon-Cavanagh, S., Zeinieh, M., De Jay, N., Deshmukh, S., Chen, C.C.L., Belle, J., Mikael, L.G., et al. (2019). H3K27M induces defective chromatin spread of PRC2-mediated repressive H3K27me2/me3 and is essential for glioma tumorigenesis. Nat. Commun. *10*, 1262. https://doi.org/10.1038/s41467-019-09140-x.
12. Pajtler, K.W., Wen, J., Sill, M., Lin, T., Orisme, W., Tang, B., Hübner, J.-M., Ramaswamy, V., Jia, S., Dalton, J.D., et al. (2018). Molecular heterogeneity and CXorf67 alterations in posterior fossa group A (PFA) ependymomas. Acta Neuropathol. *136*, 211–226. https://doi.org/10.1007/s00401-018-1877-0.
13. Belton, J.-M., McCord, R.P., Gibcus, J.H., Naumova, N., Zhan, Y., and Dekker, J. (2012). Hi-C: a comprehensive technique to capture the conformation of genomes. Methods (San Diego, Calif.) *58*, 268–276. https://doi.org/10.1016/j.ymeth.2012.05.001.
14. Lieberman-Aiden, E., Van Berkum, N.L., Williams, L., Imakaev, M., Ragoczy, T., Telling, A., Amit, I., Lajoie, B.R., Sabo, P.J., Dorschner, M.O., et al. (2009). Comprehensive mapping of long-range interactions reveals folding principles of the human genome. Science (New York, N.Y.) *326*, 289–293. https://doi.org/10.1126/science.1181369.
15. Rao, S.S.P., Huntley, M.H., Durand, N.C., Stamenova, E.K., Bochkov, I.D., Robinson, J.T., Sanborn, A.L., Machol, I., Omer, A.D., Lander, E.S., and Aiden, E.L. (2014). A 3D map of the human genome at kilobase resolution reveals principles of chromatin looping. Cell *159*, 1665–1680. https://doi.org/10.1016/j.cell.2014.11.021.
16. Dixon, J.R., Selvaraj, S., Yue, F., Kim, A., Li, Y., Shen, Y., Hu, M., Liu, J.S., and Ren, B. (2012). Topological domains in mammalian genomes identified by analysis of chromatin interactions. Nature *485*, 376–380. https://doi.org/10.1038/nature11082.
17. Stevens, T.J., Lando, D., Basu, S., Atkinson, L.P., Cao, Y., Lee, S.F., Leeb, M., Wohlfahrt, K.J., Boucher, W., O'Shaughnessy-Kirwan, A., et al. (2017). 3D structures of individual mammalian genomes studied by single-cell Hi-C. Nature *544*, 59–64. https://doi.org/10.1038/nature21429.
18. Lupiáñez, D.G., Kraft, K., Heinrich, V., Krawitz, P., Brancati, F., Klopocki, E., Horn, D., Kayserili, H., Opitz, J.M., Laxova, R., et al. (2015). Disruptions of topological chromatin domains cause pathogenic rewiring of gene-enhancer interactions. Cell *161*, 1012–1025. https://doi.org/10.1016/j.cell.2015.04.004.
19. Rhie, S.K., Perez, A.A., Lay, F.D., Schreiner, S., Shi, J., Polin, J., and Farnham, P.J. (2019). A high-resolution 3D epigenomic map reveals insights into the creation of the prostate cancer transcriptome. Nat. Commun. *10*, 4154. https://doi.org/10.1038/s41467-019-12079-8.
20. Zhou, Y., Gerrard, D.L., Wang, J., Li, T., Yang, Y., Fritz, A.J., Rajendran, M., Fu, X., Stein, G., Schiff, R., et al. (2019). Temporal dynamic reorganization of 3D chromatin architecture in hormone-induced breast cancer and endocrine resistance. Nat. Commun. *10*, 1522. https://doi.org/10.1038/s41467-019-09320-9.
21. Wang, J., Huang, T.Y.-T., Hou, Y., Bartom, E., Lu, X., Shilatifard, A., Yue, F., and Saratsis, A. (2021). Epigenomic landscape and 3D genome structure in pediatric high-grade glioma. Sci. Adv. *7*, eabg4126. https://doi.org/10.1126/sciadv.abg4126.
22. Flavahan, W.A., Drier, Y., Liau, B.B., Gillespie, S.M., Venteicher, A.S., Stemmer-Rachamimov, A.O., Suvà, M.L., and Bernstein, B.E. (2016). Insulator dysfunction and oncogene activation in IDH mutant gliomas. Nature *529*, 110–114. https://doi.org/10.1038/nature16490.
23. Northcott, P.A., Buchhalter, I., Morrissy, A.S., Hovestadt, V., Weischenfeldt, J., Ehrenberger, T., Gröbner, S., Segura-Wang, M., Zichner, T., Rudneva, V.A., et al. (2017). The whole-genome landscape of medulloblastoma subtypes. Nature *547*, 311–317. https://doi.org/10.1038/nature22973.
24. Johnston, M.J., Nikolic, A., Ninkovic, N., Guilhamon, P., Cavalli, F.M.G., Seaman, S., Zemp, F.J., Lee, J., Abdelkareem, A., Ellestad, K., et al. (2019). High-resolution structural genomics reveals new therapeutic vulnerabilities in glioblastoma. Genome Res. *29*, 1211–1222. https://doi.org/10.1101/gr.246520.118.
25. Won, H., de la Torre-Ubieta, L., Stein, J.L., Parikshak, N.N., Huang, J., Opland, C.K., Gandal, M.J., Sutton, G.J., Hormozdiari, F., Lu, D., et al. (2016). Chromosome conformation elucidates regulatory relationships in

developing human brain. Nature *538*, 523–527. https://doi.org/10.1038/nature19847.

26. Durand, N.C., Robinson, J.T., Shamim, M.S., Machol, I., Mesirov, J.P., Lander, E.S., and Aiden, E.L. (2016). Juicebox Provides a Visualization System for Hi-C Contact Maps with Unlimited Zoom. Cell Syst. *3*, 99–101. https://doi.org/10.1016/j.cels.2015.07.012.
27. Roayaei Ardakany, A., Gezer, H.T., Lonardi, S., and Ay, F. (2020). Mustache: multi-scale detection of chromatin loops from Hi-C and Micro-C maps using scale-space representation. Genome Biol. *21*, 256. https://doi.org/10.1186/s13059-020-02167-0.
28. Matthey-Doret, C., Baudry, L., Breuer, A., Montagne, R., Guiglielmoni, N., Scolari, V., Jean, E., Campeas, A., Chanut, P.H., Oriol, E., et al. (2020). Computer vision for pattern detection in chromosome contact maps. Nat. Commun. *11*, 5795. https://doi.org/10.1038/s41467-020-19562-7.
29. Soler-Vila, P., Cuscó, P., Farabella, I., Di Stefano, M., and Marti-Renom, M.A. (2020). Hierarchical chromatin organization detected by TADpole. Nucleic Acids Res. *48*, e39. https://doi.org/10.1093/nar/gkaa087.
30. Dali, R., Bourque, G., and Blanchette, M. (2018). RobusTAD: A Tool for Robust Annotation of Topologically Associating Domain Boundaries. Preprint at bioRxiv. https://doi.org/10.1101/293175.
31. Wang, B., Mezlini, A.M., Demir, F., Fiume, M., Tu, Z., Brudno, M., Haibe-Kains, B., and Goldenberg, A. (2014). Similarity network fusion for aggregating data types on a genomic scale. Nat. Methods *11*, 333–337. https://doi.org/10.1038/nmeth.2810.
32. Sahin, M., Wong, W., Zhan, Y., Van Deynze, K., Koche, R., and Leslie, C.S. (2021). HiC-DC+ enables systematic 3D interaction calls and differential analysis for Hi-C and HiChIP. Nat. Commun. *12*, 3366. https://doi.org/10.1038/s41467-021-23749-x.
33. Kovaka, S., Zimin, A.V., Pertea, G.M., Razaghi, R., Salzberg, S.L., and Pertea, M. (2019). Transcriptome assembly from long-read RNA-seq alignments with StringTie2. Genome Biol. *20*, 278. https://doi.org/10.1186/s13059-019-1910-1.
34. Whyte, W.A., Orlando, D.A., Hnisz, D., Abraham, B.J., Lin, C.Y., Kagey, M.H., Rahl, P.B., Lee, T.I., and Young, R.A. (2013). Master transcription factors and mediator establish super-enhancers at key cell identity genes. Cell *153*, 307–319. https://doi.org/10.1016/j.cell.2013.03.035.
35. Lovén, J., Hoke, H.A., Lin, C.Y., Lau, A., Orlando, D.A., Vakoc, C.R., Bradner, J.E., Lee, T.I., and Young, R.A. (2013). Selective inhibition of tumor oncogenes by disruption of super-enhancers. Cell *153*, 320–334. https://doi.org/10.1016/j.cell.2013.03.036.
36. Schwarzer, W., Abdennur, N., Goloborodko, A., Pekowska, A., Fudenberg, G., Loe-Mie, Y., Fonseca, N.A., Huber, W., Haering, C.H., Mirny, L., and Spitz, F. (2017). Two independent modes of chromatin organization revealed by cohesin removal. Nature *551*, 51–56. https://doi.org/10.1038/nature24281.
37. Belaghzal, H., Borrman, T., Stephens, A.D., Lafontaine, D.L., Venev, S.V., Weng, Z., Marko, J.F., and Dekker, J. (2021). Liquid chromatin Hi-C characterizes compartment-dependent chromatin interaction dynamics. Nat. Genet. *53*, 367–378. https://doi.org/10.1038/s41588-021-00784-4.
38. Todd, S., Todd, P., McGowan, S.J., Hughes, J.R., Kakui, Y., Leymarie, F.F., Latham, W., and Taylor, S. (2021). CSynth: an interactive modelling and visualization tool for 3D chromatin structure. Bioinformatics *37*, 951–955. https://doi.org/10.1093/bioinformatics/btaa757.
39. Hua, N., Tjong, H., Shin, H., Gong, K., Zhou, X.J., and Alber, F. (2018). Producing genome structure populations with the dynamic and automated PGS software. Nat. Protoc. *13*, 915–926. https://doi.org/10.1038/nprot.2018.008.
40. Wang, X., Xu, J., Zhang, B., Hou, Y., Song, F., Lyu, H., and Yue, F. (2021). Genome-wide detection of enhancer-hijacking events from chromatin interaction data in rearranged genomes. Nat. Methods *18*, 661–668. https://doi.org/10.1038/s41592-021-01164-w.
41. Liu, Y., Nanni, L., Sungalee, S., Zufferey, M., Tavernari, D., Mina, M., Ceri, S., Oricchio, E., and Ciriello, G. (2021). Systematic inference and comparison of multi-scale chromatin sub-compartments connects spatial organization to cell phenotypes. Nat. Commun. *12*, 2439. https://doi.org/10.1038/s41467-021-22666-3.
42. Mack, S.C., Pajtler, K.W., Chavez, L., Okonechnikov, K., Bertrand, K.C., Wang, X., Erkek, S., Federation, A., Song, A., Lee, C., et al. (2018). Therapeutic targeting of ependymoma as informed by oncogenic enhancer profiling. Nature *553*, 101–105. https://doi.org/10.1038/nature25169.
43. Groh, S., and Schotta, G. (2017). Silencing of endogenous retroviruses by heterochromatin. Cell. Mol. Life Sci. *74*, 2055–2065. https://doi.org/10.1007/s00018-017-2454-8.
44. Falk, M., Feodorova, Y., Naumova, N., Imakaev, M., Lajoie, B.R., Leonhardt, H., Joffe, B., Dekker, J., Fudenberg, G., Solovei, I., and Mirny, L.A. (2019). Heterochromatin drives compartmentalization of inverted and conventional nuclei. Nature *570*, 395–399. https://doi.org/10.1038/s41586-019-1275-3.
45. Dixon, J.R., Jung, I., Selvaraj, S., Shen, Y., Antosiewicz-Bourget, J.E., Lee, A.Y., Ye, Z., Kim, A., Rajagopal, N., Xie, W., et al. (2015). Chromatin architecture reorganization during stem cell differentiation. Nature *518*, 331–336. https://doi.org/10.1038/nature14222.
46. Gallo, M., Coutinho, F.J., Vanner, R.J., Gayden, T., Mack, S.C., Murison, A., Remke, M., Li, R., Takayama, N., Desai, K., et al. (2015). MLL5 Orchestrates a Cancer Self-Renewal State by Repressing the Histone Variant H3.3 and Globally Reorganizing Chromatin. Cancer Cell *28*, 715–729. https://doi.org/10.1016/j.ccell.2015.10.005.
47. Keenan, C.R., Coughlan, H.D., Iannarella, N., Johanson, T.M., Chan, W.F., Garnham, A.L., Smyth, G.K., and Allan, R.S. (2020). Suv39h-catalysed H3K9me3 is critical for euchromatic genome organisation and the maintenance of gene transcription. Preprint at bioRxiv. https://doi.org/10.1101/2020.08.13.249078.
48. Rao, S.S.P., Huang, S.-C., Glenn St Hilaire, B., Engreitz, J.M., Perez, E.M., Kieffer-Kwon, K.-R., Sanborn, A.L., Johnstone, S.E., Bascom, G.D., Bochkov, I.D., et al. (2017). Cohesin Loss Eliminates All Loop Domains. Cell *171*, 305–320.e24. https://doi.org/10.1016/j.cell.2017.09.026.
49. Nora, E.P., Goloborodko, A., Valton, A.-L., Gibcus, J.H., Uebersohn, A., Abdennur, N., Dekker, J., Mirny, L.A., and Bruneau, B.G. (2017). Targeted Degradation of CTCF Decouples Local Insulation of Chromosome Domains from Genomic Compartmentalization. Cell *169*, 930–944.e22. https://doi.org/10.1016/j.cell.2017.05.004.
50. Akdemir, K.C., Le, V.T., Kim, J.M., Killcoyne, S., King, D.A., Lin, Y.-P., Tian, Y., Inoue, A., Amin, S.B., Robinson, F.S., et al. (2020). Somatic mutation distributions in cancer genomes vary with three-dimensional chromatin structure. Nat. Genet. *52*, 1178–1188. https://doi.org/10.1038/s41588-020-0708-0.
51. Marchal, C., Sima, J., and Gilbert, D.M. (2019). Control of DNA replication timing in the 3D genome. Nat. Rev. Mol. Cell Biol. *20*, 721–737. https://doi.org/10.1038/s41580-019-0162-y.
52. Michealraj, K.A., Kumar, S.A., Kim, L.J.Y., Cavalli, F.M.G., Przelicki, D., Wojcik, J.B., Delaidelli, A., Bajic, A., Saulnier, O., MacLeod, G., et al. (2020). Metabolic Regulation of the Epigenome Drives Lethal Infantile Ependymoma. Cell *181*, 1329–1345.e24. https://doi.org/10.1016/j.cell.2020.04.047.
53. Li, H., and Durbin, R. (2009). Fast and accurate short read alignment with Burrows-Wheeler transform. Bioinformatics *25*, 1754–1760. https://doi.org/10.1093/bioinformatics/btp324.
54. Abdennur, N., and Mirny, L.A. (2020). Cooler: scalable storage for Hi-C data and other genomically labeled arrays. Bioinformatics *36*, 311–316. https://doi.org/10.1093/bioinformatics/btz540.
55. Vidal, E., le Dily, F., Quilez, J., Stadhouders, R., Cuartero, Y., Graf, T., Marti-Renom, M.A., Beato, M., and Filion, G.J. (2018). OneD: increasing reproducibility of Hi-C samples with abnormal karyotypes. Nucleic Acids Res. *46*, e49. https://doi.org/10.1093/nar/gky064.

56. Humphrey, W., Dalke, A., and Schulten, K. (1996). VMD: visual molecular dynamics. J. Mol. Graph. *14*. 33-8, 27-8. https://doi.org/10.1016/0263-7855(96)00018-5.

57. Love, M.I., Huber, W., and Anders, S. (2014). Moderated estimation of fold change and dispersion for RNA-seq data with DESeq2. Genome Biol. *15*, 550. https://doi.org/10.1186/s13059-014-0550-8.

58. Quinlan, A.R., and Hall, I.M. (2010). BEDTools: A flexible suite of utilities for comparing genomic features. Bioinformatics *26*, 841–842. https://doi.org/10.1093/bioinformatics/btq033.

59. Flyamer, I.M., Illingworth, R.S., and Bickmore, W.A. (2020). Coolpup.py: versatile pile-up analysis of Hi-C data. Bioinformatics *36*, 2980–2985. https://doi.org/10.1093/bioinformatics/btaa073.

60. Ghandi, M., Mohammad-Noori, M., Ghareghani, N., Lee, D., Garraway, L., and Beer, M.A. (2016). gkmSVM: an R package for gapped-kmer SVM. Bioinformatics *32*, 2205–2207. https://doi.org/10.1093/bioinformatics/btw203.

61. Ramírez, F., Ryan, D.P., Grüning, B., Bhardwaj, V., Kilpert, F., Richter, A.S., Heyne, S., Dündar, F., and Manke, T. (2016). deepTools2: a next generation web server for deep-sequencing data analysis. Nucleic Acids Res. *44*, W160–W165. https://doi.org/10.1093/nar/gkw257.

62. Kim, D., Paggi, J.M., Park, C., Bennett, C., and Salzberg, S.L. (2019). Graph-based genome alignment and genotyping with HISAT2 and HISAT-genotype. Nat. Biotechnol. *37*, 907–915. https://doi.org/10.1038/s41587-019-0201-4.

63. Li, H., Handsaker, B., Wysoker, A., Fennell, T., Ruan, J., Homer, N., Marth, G., Abecasis, G., and Durbin, R.; 1000 Genome Project Data Processing Subgroup (2009). The Sequence Alignment/Map format and SAMtools. Bioinformatics *25*, 2078–2079. https://doi.org/10.1093/bioinformatics/btp352.

64. Anders, S., Pyl, P.T., and Huber, W. (2015). HTSeq–a Python framework to work with high-throughput sequencing data. Bioinformatics *31*, 166–169. https://doi.org/10.1093/bioinformatics/btu638.

65. Ritchie, M.E., Phipson, B., Wu, D., Hu, Y., Law, C.W., Shi, W., and Smyth, G.K. (2015). limma powers differential expression analyses for RNA-sequencing and microarray studies. Nucleic Acids Res. *43*, e47. https://doi.org/10.1093/nar/gkv007.

66. Pertea, M., Pertea, G.M., Antonescu, C.M., Chang, T.-C., Mendell, J.T., and Salzberg, S.L. (2015). StringTie enables improved reconstruction of a transcriptome from RNA-seq reads. Nat. Biotechnol. *33*, 290–295. https://doi.org/10.1038/nbt.3122.

67. Pertea, M., Kim, D., Pertea, G.M., Leek, J.T., and Salzberg, S.L. (2016). Transcript-level expression analysis of RNA-seq experiments with HISAT, StringTie and Ballgown. Nat. Protoc. *11*, 1650–1667. https://doi.org/10.1038/nprot.2016.095.

68. Pertea, G., and Pertea, M. (2020). GFF Utilities: GffRead and GffCompare. F1000Res. *9*. ISCB Comm J-304. https://doi.org/10.12688/f1000research.23297.2.

69. Bray, N.L., Pimentel, H., Melsted, P., and Pachter, L. (2016). Near-optimal probabilistic RNA-seq quantification. Nat. Biotechnol. *34*, 525–527. https://doi.org/10.1038/nbt.3519.

70. Zhang, A.W., O'Flanagan, C., Chavez, E.A., Lim, J.L.P., Ceglia, N., McPherson, A., Wiens, M., Walters, P., Chan, T., Hewitson, B., et al. (2019). Probabilistic cell-type assignment of single-cell RNA-seq for tumor microenvironment profiling. Nat. Methods *16*, 1007–1015. https://doi.org/10.1038/s41592-019-0529-1.

71. Newman, A.M., Steen, C.B., Liu, C.L., Gentles, A.J., Chaudhuri, A.A., Scherer, F., Khodadoust, M.S., Esfahani, M.S., Luca, B.A., Steiner, D., et al. (2019). Determining cell type abundance and expression from bulk tissues with digital cytometry. Nat. Biotechnol. *37*, 773–782. https://doi.org/10.1038/s41587-019-0114-2.

72. Krueger, F., and Andrews, S.R. (2011). Bismark: a flexible aligner and methylation caller for Bisulfite-Seq applications. Bioinformatics *27*, 1571–1572. https://doi.org/10.1093/bioinformatics/btr167.

73. Hao, Z., Lv, D., Ge, Y., Shi, J., Weijers, D., Yu, G., and Chen, J. (2020). RIdeogram: drawing SVG graphics to visualize and map genome-wide data on the idiograms. PeerJ. Comput. Sci. *6*, e251. https://doi.org/10.7717/peerj-cs.251.

74. Ramírez, F., Bhardwaj, V., Arrigoni, L., Lam, K.C., Grüning, B.A., Villaveces, J., Habermann, B., Akhtar, A., and Manke, T. (2018). High-resolution TADs reveal DNA sequences underlying genome organization in flies. Nat. Commun. *9*, 189. https://doi.org/10.1038/s41467-017-02525-w.

75. Lopez-Delisle, L., Rabbani, L., Wolff, J., Bhardwaj, V., Backofen, R., Grüning, B., Ramírez, F., and Manke, T. (2021). pyGenomeTracks: reproducible plots for multivariate genomic datasets. Bioinformatics *37*, 422–423. https://doi.org/10.1093/bioinformatics/btaa692.

76. Robinson, J.T., Thorvaldsdóttir, H., Winckler, W., Guttman, M., Lander, E.S., Getz, G., and Mesirov, J.P. (2011). Integrative genomics viewer. Nat. Biotechnol. *29*, 24–26. https://doi.org/10.1038/nbt.1754.

77. Li, H. (2018). Minimap2: pairwise alignment for nucleotide sequences. Bioinformatics *34*, 3094–3100. https://doi.org/10.1093/bioinformatics/bty191.

78. Heller, D., and Vingron, M. (2019). SVIM: structural variant identification using mapped long reads. Bioinformatics *35*, 2907–2915. https://doi.org/10.1093/bioinformatics/btz041.

79. Zhang, Y., Liu, T., Meyer, C.A., Eeckhoute, J., Johnson, D.S., Bernstein, B.E., Nusbaum, C., Myers, R.M., Brown, M., Li, W., and Liu, X.S. (2008). Model-based analysis of ChIP-Seq (MACS). Genome Biol. *9*, R137. https://doi.org/10.1186/gb-2008-9-9-r137.

80. Yang, T., Zhang, F., Yardımcı, G.G., Song, F., Hardison, R.C., Noble, W.S., Yue, F., and Li, Q. (2017). HiCRep: assessing the reproducibility of Hi-C data using a stratum-adjusted correlation coefficient. Genome Res. *27*, 1939–1949. https://doi.org/10.1101/gr.220640.117.

81. Durand, N.C., Shamim, M.S., Machol, I., Rao, S.S.P., Huntley, M.H., Lander, E.S., and Aiden, E.L. (2016). Juicer Provides a One-Click System for Analyzing Loop-Resolution Hi-C Experiments. Cell Syst. *3*, 95–98. https://doi.org/10.1016/j.cels.2016.07.002.

82. Roadmap Epigenomics Consortium, Kundaje, A., Meuleman, W., Ernst, J., Bilenky, M., Yen, A., Heravi-Moussavi, A., Kheradpour, P., Zhang, Z., Wang, J., et al. (2015). Integrative analysis of 111 reference human epigenomes. Nature *518*, 317–330. https://doi.org/10.1038/nature14248.

83. Imakaev, M., Fudenberg, G., McCord, R.P., Naumova, N., Goloborodko, A., Lajoie, B.R., Dekker, J., and Mirny, L.A. (2012). Iterative correction of Hi-C data reveals hallmarks of chromosome organization. Nat. Methods *9*, 999–1003. https://doi.org/10.1038/nmeth.2148.

84. Zerbino, D.R., Wilder, S.P., Johnson, N., Juettemann, T., and Flicek, P.R. (2015). The ensembl regulatory build. Genome Biol. *16*, 56. https://doi.org/10.1186/s13059-015-0621-5.

85. Boninsegna, L., Yildirim, A., Polles, G., Zhan, Y., Quinodoz, S.A., Finn, E.H., Guttman, M., Zhou, X.J., and Alber, F. (2022). Integrative genome modeling platform reveals essentiality of rare contact events in 3D genome organizations. Nat. Methods *19*, 938–949. https://doi.org/10.1038/s41592-022-01527-x.

86. Frankish, A., Diekhans, M., Ferreira, A.-M., Johnson, R., Jungreis, I., Loveland, J., Mudge, J.M., Sisu, C., Wright, J., Armstrong, J., et al. (2019). GENCODE reference annotation for the human and mouse genomes. Nucleic Acids Res. *47*, D766–D773. https://doi.org/10.1093/nar/gky955.

87. Parker, M., Mohankumar, K.M., Punchihewa, C., Weinlich, R., Dalton, J.D., Li, Y., Lee, R., Tatevossian, R.G., Phoenix, T.N., Thiruvenkatam, R., et al. (2014). C11orf95-RELA fusions drive oncogenic NF-κB signalling in ependymoma. Nature *506*, 451–455. https://doi.org/10.1038/nature13109.

88. Wu, G., Diaz, A.K., Paugh, B.S., Rankin, S.L., Ju, B., Li, Y., Zhu, X., Qu, C., Chen, X., Zhang, J., et al. (2014). The genomic landscape of diffuse intrinsic pontine glioma and pediatric non-brainstem high-grade glioma. Nat. Genet. *46*, 444–450. https://doi.org/10.1038/ng.2938.

89. McLeod, C., Gout, A.M., Zhou, X., Thrasher, A., Rahbarinia, D., Brady, S.W., Macias, M., Birch, K., Finkelstein, D., Sunny, J., et al. (2021). St.

Jude Cloud: A Pediatric Cancer Genomic Data-Sharing Ecosystem. Cancer Discov. *11*, 1082–1099. https://doi.org/10.1158/2159-8290.CD-20-1230.

90. Gojo, J., Englinger, B., Jiang, L., Hübner, J.M., Shaw, M.L., Hack, O.A., Madlener, S., Kirchhofer, D., Liu, I., Pyrdol, J., et al. (2020). Single-Cell RNA-Seq Reveals Cellular Hierarchies and Impaired Developmental Trajectories in Pediatric Ependymoma. Cancer Cell *38*, 44–59.e9. https://doi.org/10.1016/j.ccell.2020.06.004.

91. Madani Tonekaboni, S.A., Mazrooei, P., Kofia, V., Haibe-Kains, B., and Lupien, M. (2019). Identifying clusters of cis-regulatory elements underpinning TAD structures and lineage-specific regulatory networks. Genome Res. *29*, 1733–1743. https://doi.org/10.1101/gr.248658.119.

92. Richardson, S.O., Huibers, M.M.H., de Weger, R.A., de Leng, W.W.J., Hinrichs, J.W.J., Meijers, R.W.J., Willems, S.M., and Peeters, T.L.M.G. (2019). One-fits-all pretreatment protocol facilitating Fluorescence In Situ Hybridization on formalin-fixed paraffin-embedded, fresh frozen and cytological slides. Mol. Cytogenet. *12*, 27. https://doi.org/10.1186/s13039-019-0442-4.

Please cite this article in press as: Johnston et al., TULIPs decorate the three-dimensional genome of PFA ependymoma, Cell (2024), https://doi.org/10.1016/j.cell.2024.06.023

CellPress
OPEN ACCESS

STAR★METHODS

KEY RESOURCES TABLE

REAGENT or RESOURCE	SOURCE	IDENTIFIER
Antibodies		
H3K9me3 antibody (Active motif)	Active Motif	Cat# 39161; RRID: AB_2532132
H3K27me3 antibody (Diagenode)	Diagenode	Cat# C15410069; RRID: AB_2814977
H3K27me3 antibody (Cell Signaling)	Cell Signaling	Cat# CST 9733
H3K9me3 antibody (Abcam)	Abcam	Cat# Ab8898; RRID: AB_306848
Invitrogen goat anti rabbit antibody Alexa 647	Invitrogen	Cat# A-21245
Goat Anti-HP1alpha antibody (ChIP grade)	Abcam	Cat# Ab77256; RRID: AB_1523784
Mouse HP1gamma Monoclonal Antibody	Thermo Fisher Scientific	Cat# 2MOD-1G6
Donkey anti-Rabbit IgG (H + L), Alexa Fluor™ 647	Thermo Fisher Scientific	Cat# A31573; RRID: AB_2536183
Donkey anti-goat IgG (H + L), Alexa Fluor™ 647	Thermo Fisher Scientific	Cat# A21447; RRID: AB_2535864
Goat anti-Mouse IgG (H + L) Cross-Adsorbed Secondary Antibody, Alexa Fluor™ 488	Thermo Fisher Scientific	Cat# A-11001; RRID: AB_2534069
Rabbit anti-EZHIP polyclonal antibody	Millipore	Cat# ABC1378
Histone H3 K27Ac Antibody	Active Motif	Cat# 39134; RRID: AB_2722569
Goat anti-rabbit IgG H&L (hrp)	Abcam	Cat# ab6721; RRID: AB_955447
Biological samples		
Tissue – primary medulloblastoma	This paper	N/A
Tissue – primary ependymoma (PFA, PFB, ST)	This paper	N/A
Tissue – primary pediatric glioma	This paper	N/A
FFPE blocks for brain tumor tissues	This paper	N/A
Chemicals, peptides, and recombinant proteins		
DAPI	Thermo Fisher Scientific	Cat# 62248
Prolong Diamond Antifade	Life Technologies	Cat# P36965
EGF	Sigma-Aldrich	Cat# E9644
FGF	Peprotech	Cat# 100-18B
Heparin	Sigma-Aldrich	Cat# H3393
NeuroCult NS-A Basal Medium (Human)	Stemcell Technologies Inc.	Cat# 05750
N2 Supplement (100X)	Thermo Fisher Scientific	Cat# 17502048
B27 Supplement (50X), minus vitamin A	Thermo Fisher Scientific	Cat# 12587010
Glutamax	Thermo Fisher Scientific	Cat# 35050061
BSA	Sigma-Aldrich	
NeuroCult™ Proliferation Supplement (Human)	Stemcell Technologies Inc.	Cat# 05753
poly-L-ornithine	Sigma-Aldrich	Cat# P4957
laminin	Sigma-Aldrich	Cat# L2020
1,6-hexanediol	Sigma-Aldrich	Cat# 240117-50G
UNC0642	Structural Genomics Consortium	N/A
A366	Structural Genomics Consortium	N/A
Chaetocin	Cayman Chemical	Cat# 28097-03-2
Alamar blue	Thermo Fisher Scientific	Cat# DAL1025
Piggybac transposase	System Biosciences	Cat# PB210PA-1
Critical commercial assays		
Detergent compatible protein assay	Bio-Rad	Cat# 5000112
dsDNA BR Assay Kit	Thermo Fisher Scientific	Cat# Q32853
Femto Pulse	Agilent Technologies	Cat# FP-1002-0275

(*Continued on next page*)

Please cite this article in press as: Johnston et al., TULIPs decorate the three-dimensional genome of PFA ependymoma, Cell (2024), https://doi.org/10.1016/j.cell.2024.06.023

Continued

REAGENT or RESOURCE	SOURCE	IDENTIFIER
ClickIT™ Plus EdU Cell Proliferation, Alexa Fluor™ 647 Imaging Kit	Thermo Fisher Scientific	Cat# C10640
mouse neural stem cell nucleofection kit	Lonza	Cat# VPG-1004
Deposited data		
Gene Expression Omnibus (GEO): GSE186599	This paper	N/A
Mendeley Data: http://doi.org/10.17632/k4x43trfd9.1	This paper	N/A
European Genome-Phenome Archive (EGA): EGAS00001005476	This paper	N/A
Experimental models: Cell lines		
Primary cell cultures - MDT-PFA EPN	Michealraj et al.[52]	N/A
Oligonucleotides		
Custom oligo-FISH probes against compartment B regions (chr8:34200000–35500000, chr8:394500000–39800000, chr8:43250000-43750000), tagged with ATTO-647	This paper; myTags, Arbor Biosciences	N/A
Custom oligo-FISH probes against compartment A regions (chr8:3775000–38450000, chr8:41500000-42050000), tagged with Alexa 488	This paper; myTags, Arbor Biosciences	N/A
Recombinant DNA		
pPB[Exp]-Puro-EF1A > hEZHIP [NM_203407.3] construct	This paper; Vector Builder	VB220623-1246rfk
pPB[Exp]-Puro-EF1A>TurboRFP	This paper; Vector Builder	VB900129-0773jdw
EF1a-EZHIP (WT)-turboRFP-Luc	Jain et al.[5]	N/A
EF1a-EZHIP (R405E)-turboRFP-Luc	Jain et al.[5]	N/A
Software and algorithms		
Juicer (v1.6), CPU	Durand et al.[26]	N/A
bwa (v0.7.17)	Li and Durbin[53]	N/A
Java (openjdk = 8.0)	https://openjdk.org/projects/jdk8/	N/A
hic2cool (v0.8.3)	https://github.com/4dn-dcic/hic2cool	N/A
cooler (v0.8.10)	Abdennur and Mirny,[54] https://github.com/open2c/cooler	N/A
RobusTAD (v1.0)	Dali et al.[30]	N/A
Juicer Tools (v1.19.02)	https://github.com/aidenlab/JuicerTools	N/A
OneD (commit 5b1fdae)	Vidal et al.,[55] https://github.com/qenvio/dryhic	N/A
TADpole (commit f4b1f62)	Soler-Vila et al.,[29] https://github.com/3DGenomes/TADpole	N/A
cooltools (v0.4.0)	https://github.com/open2c/cooltools	N/A
Mustache (v1.0.1)	Roayaei Ardakani et al.,[27] https://github.com/ay-lab/mustache	N/A
Chromosight (v1.6.1)	Matthey-Doret et al.[28]	N/A
HiC-DC+ v(0.99.14)	Sahin et al.,[32] Carty et al.[56]	N/A
DESeq2 (v1.30.1)	Love et al.[57]	N/A
bedtools (v2.26.0)	Quinlan et al.[58]	N/A
ImageMagick (v7.0.10_28)	https://imagemagick.org	N/A
Coolpup (v0.9.5)	Flyamer et al.[59]	N/A
NeoLoopFinder (v0.2.3)	Wang et al.[40]	N/A
Pairtools (v0.3.0)	https://github.com/open2c/pairtools	N/A
CALDER (v0.1)	Liu et al.[41]	N/A

(*Continued on next page*)

Please cite this article in press as: Johnston et al., TULIPs decorate the three-dimensional genome of PFA ependymoma, Cell (2024), https://doi.org/10.1016/j.cell.2024.06.023

Continued

REAGENT or RESOURCE	SOURCE	IDENTIFIER
gkmSVM (v0.81.0)	Ghandi et al.[60]	N/A
deepTools v3.5.1	Ramirez et al.[61]	N/A
VMD (v1.9.3)	Humphrey et al.[56]	N/A
HISAT2 (v2.1.0)	Kim et al.[62]	N/A
Samtools v1.9	Li et al.[63]	N/A
HTSeq (v0.13)	Anders et al.[64]	N/A
Limma (v3.44)	Ritchie et al.[65]	N/A
StringTie (v2.0)	Pertea et al.[66,67]	N/A
GffCompare (v 0.11.7)	Pertea et al.[68]	N/A
GffRead (v0.11.7)	Pertea et al.[68]	N/A
kallisto (v 0.45.1)	Bray et al.[69]	N/A
CellAssign (v0.99)	Zhang et al.[70]	N/A
CIBERSORTx (web interface)	Newman et al.[71]	N/A
Bismark (v0.22.3)	Krueger et al.[72]	N/A
ROSE (v1.2.0)	Whyte et al.,[34] Loven et al.[35]	N/A
R (v4.0.3)	https://cran.r-project.org/bin/windows/base/old/4.0.3/	N/A
broom (v0.7.5)	https://broom.tidymodels.org/	N/A
hexbin (v1.28.2)	https://github.com/edzer/hexbin	N/A
ggpubr (v0.4.0)	https://rpkgs.datanovia.com/ggpubr/	N/A
RColorBrewer (v1.1.2)	https://cran.r-project.org/web/packages/RColorBrewer/index.html	N/A
tidyverse (v1.3.0)	https://www.tidyverse.org/	N/A
RIdeogram (v0.2.2)	Hao et al.[73]	N/A
NMF (v0.21.0)	https://renozao.github.io/NMF/	N/A
R (3.6.3)	https://cran-archive.r-project.org/bin/windows/base/old/3.6.3/	N/A
optparse (v1.6.6)	https://github.com/python/cpython/blob/3.12/Lib/optparse.py	N/A
Juicebox (v1.11.08)	Durand et al.[26]	N/A
HiCExplorer (v3.7.2)	Ramirez et al.[74]	N/A
pyGenomeTracks (v3.6)	Lopez-Delisle et al.[75]	N/A
IGV (v2.12.3)	Robinson et al.[76]	N/A
Guppy (v4.0.11)	Oxford Nanopore Technologies; https://community.nanoporetech.com/downloads	N/A
minimap2 (v2.17)	Li[77]	N/A
PycoQC (v2.5.2)	https://github.com/tleonardi/pycoQC	N/A
SVIM (v1.2.0)	Heller and Vingron[78]	N/A
MACS2 (v2.1.2)	Zhang et al.,[79] https://github.com/macs3-project/MACS	N/A
HiCRep (v0.2.5)	Yang et al.[80]	N/A
Other		
Kapa HyperPrep Kit	Roche	Cat# KR0961
Mini-PROTEAN gels	Bio-Rad	Cat# 4568044
12% Mini-PROTEAN gels	Bio-Rad	Cat# 4568045
Nanobind Tissue Big DNA Kit	Circulomics	Cat# NB-900-701-01
Short read eliminator kit	Circulomics	Cat# SS-100-101-01
Nanopore Ligation Sequencing Kit	Oxford Nanopore Technologies	Cat# SQK-LSK110
PromethION flow cells	Oxford Nanopore Technologies	Cat# FLO-PRO002
18 Well μ-Slide Glass Bottom	Ibidi	Cat# 81817

Please cite this article in press as: Johnston et al., TULIPs decorate the three-dimensional genome of PFA ependymoma, Cell (2024), https://doi.org/10.1016/j.cell.2024.06.023

RESOURCE AVAILABILITY

Lead contact

Further information and requests for resources and reagents should be directed to the lead contact, Marco Gallo (marco.gallo@bcm.edu).

Materials availability

Plasmids generated in this study may be made available upon reasonable request following institutional approval of a material transfer agreement (MTA).

Data and code availability

- All processed data have been deposited at GEO and are publicly available as of the date of publication. Restricted data (i.e., raw Hi-C sequencing files) have been uploaded at EGA. Accession numbers are listed in the key resources table. Original western blot images have been deposited at Mendeley and are publicly available as of the date of publication. The DOI is listed in the key resources table. Microscopy data reported in this paper will be shared by the lead contact upon request.
- This paper does not report original code.
- Any additional information required to reanalyze the data reported in this paper is available from the lead contact upon request.

EXPERIMENTAL MODEL AND STUDY PARTICIPANT DETAILS

Human samples

Primary tumors used in the study were collected and processed after receiving written informed consent based on the guidelines from Research Ethics Board from the following institutes: Hospital for Sick Children (Toronto, Canada) and McGill University (Montreal, Canada). Statistical methods were not used to predetermine the sample size. Tumor diagnosis, biological sex and age of donor are listed in Table S1 whenever possible. Sample size descriptions are presented in Figure 1 and Table S1. Sex-based analyses are presented in the Results section. hNPC primary cultures were derived from samples obtained in accordance with a protocol approved by the Conjoint Health Research Ethics Board at the University of Calgary.

Primary cell cultures

PFA ependymoma cells were cultured as previously described[52] on adherent plates coated with laminin and poly-L-ornithine and grown in defined ependymoma culture media (serum free Human Neurocult NS-A Basal media (StemCell Technologies) which was supplemented with N2 (20 ng/mL, Life Technologies), B27 (Life Technologies), EGF (10 ng/mL Life Technologies), FGF (10 ng/mL Peprotech), heparin (2 μg/mL), BSA (300 μg/mL, Sigma-Aldrich) and 2 mM Glutamine (GlutaMAX, 75 μg/mL, Life Technologies) under hypoxic conditions. Other primary cells were cultured in a similar fashion on adherent plates, but using Human Neurocult NS-A Basal media supplemented with NS-A proliferation supplement (StemCell Technologies), EGF (10 ng/mL Life Technologies) and FGF (20 ng/mL) Peprotech and heparin (2 μg/mL; StemCell Technologies). hNPC primary cultures were grown as described above in normoxic conditions.

METHOD DETAILS

Hi-C library preparation

Fresh tissue samples were obtained from The Hospital for Sick Children (Toronto, ON) or Hospital St. Jude (Montreal). Primary cultures were grown as previously described.[52] *In situ* Hi-C[15] libraries were generated as described previously[24] using approximately 2.5 million dissociated cells as input. All Hi-C libraries were sequenced at 150 bp PE with a Hi-Seq X instrument (Illumina) at McGill Genome Center (Montreal, QC). In total, 72 Hi-C libraries were generated and sequenced, although 8 were subsequently excluded based on QC metrics (Table S1).

Hi-C data analysis

Contact maps

Juicer (v1.6, CPU)[81] was used to process Hi-C library fastqs to '.hic' format contact maps. Dependencies of the Juicer pipeline included bwa (v0.7.17)[53] and Java (openjdk = 8.0). Reads were aligned using hg38 coordinates (GCA_000001405.15_GRCh38_no_alt_plus_hs38d1_analysis_set). Samples with resolution above 15 kb (as determined by the Juicer script 'calculate_map_resolution.sh') or where less than 10% of all alignable read pairs resulted in long-range contacts (as determined from Juicer's inter_30.txt QC file) were excluded from downstream analysis.

Alongside the samples collected for this study, we reprocessed data from the developing brain[25] (dbGaP accession number phs001190.v1.p1). These data were processed equivalently to our collected samples, except for the restriction enzyme specified to Juicer; HindIII was used for the Won et al. samples, while DpnII was used for the newly collected samples.

Juicer (.hic) files were further converted to multi-resolution cooler (.mcool) files [https://github.com/open2c/cooler,[60]] using hic2-cool v0.8.3 [https://github.com/4dn-dcic/hic2cool] to take advantage of additional downstream analysis packages.

Contact domains

To annotate contact domains, hic files were processed using Juicer Tools (v1.19.02) Arrowhead with parameters '–ignore-sparsity -k SCALE' for the following data resolutions (kb): 10, 25, 50, 100. To compare Arrowhead block scores between samples, we first defined the union of all domains called across all samples. Arrowhead was subsequently re-run with the parameters 'feature_list' and 'control_list' set to this domain union to calculate block scores at all positions of interest for each sample. Alternatively, 50kb contact matrices were first corrected using OneD[61] on default settings – a method designed to account for local chromosomal abnormalities in cancer samples, after which TADpole[29] was ran with default parameters except for min_clusters = 20 to identify optimal chromosomal partitioning (i.e., TADs).

To assess boundary scores at the edges of contact domains, RobusTAD (v1.0)[30] was run with parameters '–norm = norm' on 50-kb Hi-C contact matrices generated by Juicer Tools dump with parameters '-d observed SCALE 50000 BP'. Independently, insulation scores were computed for mcool files at 10-kb resolution with a window size of 100 kb using the diamond-insulation module of cooltools v0.4.0 [https://github.com/open2c/cooltools] which implements the approach described in.[54] Boundaries were identified as bins with boundary prominence >0.2, consistent with 4DN standards.

Loops

To annotate chromatin loops, hic files were processed using Juicer Tools (v1.19.02) HiCCUPS with parameters '–cpu -m 4096 –ignore-sparsity -k SCALE' for resolutions (kb): 10, 25. To compare HiCCUPS loop scores between samples, we first defined the union of all loops called across all samples. HiCCUPS was subsequently re-run with the parameter 'specified_loop_list' set to this loop union to calculate loop scores at all positions of interest for each sample.

Independently, significant long-range interactions were identified from 10-kb contact matrices using Mustache v1.0.1 [https://github.com/ay-lab/mustache,[27]] as well as Chromosight v1.6.1[28] with default parameters. Differential interactions were determined using the hicdcdiff function from the package HiC-DC+ v0.99.14[32] built on top of DESeq2 1.30.1[57] with default parameters, where the number of contacts linking pairs of 10 kb bins were tabulated into a count matrix. Alternatively, the similarity of the submatrix surrounding putative loop pixels to an idealized "donut" loop pattern was evaluated using Chromosight's quantify module at 10 kb resolution, producing a loop score matrix analogous to the aforementioned count matrix. To assess global differences in loop strength, we compared the normalized loop interaction scores among the union set of loops called in 21 PFA samples and 10 non-PFA ependymomas. For each caller, individual loop positions were filtered to maintain with well-defined (not NA) scores for over 10 samples. Then, significance was determined using a two-sided t-test. The *p*-values were further corrected, per caller, with an FDR correction for multiple testing. A variant of this analysis was performed where loops were subdivided into three groups – inside, outside, in/out – based on how the loops overlapped TULIP loci, using Wilcoxon rank-sum test instead and without further correction.

Compartments

To annotate chromatin compartments, hic files were processed using Juicer Tools (v1.19.02) Pearsons with parameters 'SCALE 50000 BP -p' to return the correlation matrix for each chromosome. Eigenvectors for principal components 1–3 of the Pearson correlation matrix were calculated in R (v4.0.3; https://www.R-project.org/), separated into their positive and negative values, and each was compared to brain H3K27ac ChIP signal[82] (http://www.roadmapepigenomics.org/data) using 'bedtools jaccard' (v2.26.0).[58] The eigenvector with the highest jaccard similarity was selected to represent genome compartmentalization. If the highest jaccard similarity corresponded to the negative values of the eigenvector, then the eigenvector was inverted such that positive values correspond to Type A compartmentalization.

To assess predominant compartment sizes between samples, the first eigenvector of each 100-kb resolution contact matrix was computed per-arm using the call-compartments module of cooltools v0.4.0, with GC content as the reference track for sign flipping. Auto-correlation profiles were determined using the acf function from R package stats v4.0.3 with default parameters except na.action set to na.pass.

To assess interaction patterns between bins belonging to different quantiles of compartment scores, mcool files were processed using the compute-saddle module from cooltools v0.4.0 with default parameters at 100-kb resolution using eigenvectors and expected values from the call-compartments and compute-expected modules, respectively.

To quantify the contact enrichment between extreme type A and type B compartments we first identified genomic bins within the bottom 5% (type B) or top 5% (type A) of compartment eigenvalues, which correspond to the corners of the compartment saddle plots. Interactions were filtered to include only intra-chromosomal contacts separated by > 10Mb. Finally, extreme A-A, A-B, or B-B interaction strength was taken as the mean Observed/Expected values for these interactions.

TULIP interactions

To assess TULIPs, we developed a 2D pixel-based detection algorithm to identify contiguous genomic regions with frequent contacts spanning large genomic distances (Figures S3B–S3I). For each chromosome, we accessed the Observed/Expected (OE) contact matrices using Juicer Tools dump with parameters '-d oe SCALE 50000 BP'. In an approach similar to Ranked Ordering of SuperEnhancers (ROSE),[38,39] the values within the OE matrix were sorted in ascending order, and a threshold OE value was defined where the slope of OE vs. value rank was greater than 1. The threshold OE value was typically in the range 5–10, and the OE matrix was subsequently binarized to 0 or 1 using this threshold value. Separate files were generated for each combination of compartment type interactions (i.e., A-A, B-B, or A-B interactions). The binarized OE matrices were then converted to 8-bit PGM image format for

pixel-based signal smoothing in ImageMagick (v7.0.10_28; https://imagemagick.org). The command 'convert -morphology Close Diamond -morphology Open Diamond -morphology Smooth Square:3' was used to filter out dispersed or isolated signal while retaining broad, highly interconnected regions. PGM pixels were converted back to genomic bins in BEDPE and BED format, and interactions separated by less than 10 Mb were excluded. Finally, bedtools genomecov was run on the resultant BED files with parameters '-bga' to count the total number of distant bins that each bin interacts with, and bins with fewer than 10 interacting bins were excluded from the final BED file. TULIPs were defined by the BED file containing B-B type interactions.

To assess the strength of interactions between TULIP regions, we applied off-diagonal pile-up analysis to the union set of TULIP regions with genomic separation >10 Mb using coolpup.py (v0.9.5)[59] with parameters '–rescale –mindist 10000000'. A summary value of each pile-up plot ("inter-TULIP contacts") was taken as the average OE value between rescaled TULIP regions (i.e., the center 33x33 square).

To assess the effects of predicted CNVs on TULIP interactions, interaction strength was calculated both with conventional matrix normalization (ICE) and CNV-aware matrix balancing as implemented by NeoLoopFinder[40] with default parameters to take mappability, GC content, restriction fragment size, and predicted CNV profiles into account.

Comparison Hi-C datasets

To provide context for the samples in our study, we compared our in-house Hi-C data to multiple previously published datasets (Table S5). Raw Hi-C sequencing data was downloaded from the GEO repository and processed them with distiller (https://github.com/open2c/distiller-nf). Reads were mapped to hg38 using bwa mem with option -SP and the aligned reads were processed with pairtools (https://github.com/open2c/pairtools) to remove duplicates (allowing 1 bp mismatch) and low quality read pairs (MAPQ<10) to produce a set of valid read pairs. Valid pairs were binned into fixed-sized bins and created contact matrices at 1 kb, 5 kb, 50 kb resolutions using cooler.[54] Lastly, we used the cooler balance function to normalize all contact matrices using the iterative correction procedure.[83]

Biases in chromatin compartmentalization changes

CALDER was used to assign genome compartmentalization status into eight categories spanning the spectrum of chromatin accessibility ranging from most open (A.1.1) to most closed (B.2.2). CALDER was run at 50-kb resolution separately for each chromosome, then genome-wide results were merged for each sample. For each tumor subgroup, we generated subgroup-specific consensus compartmentalization calls by identifying the most frequent compartmentalization status for each bin among samples within that subgroup. In the case of two statuses being equally prevalent, one of the two most common statuses was selected randomly. We then performed pairwise comparisons between sample:sample pairs or sample:subgroup consensus pairs to quantify the number of genomic bins exhibiting each category of compartmentalization change. To summarize biases in chromatin opening or closing into a single value, we calculated the $\log_2$(open/close), where the ratio represents the number of more open bins divided by the number of more closed bins. When calculating this ratio, we excluded counts for bins that remained in the same CALDER status or shifted by only one CALDER compartmentalization category, thereby enforcing a minimum compartmentalization change of at least two CALDER categories. Two-sided t-tests were performed to assess the deviation of the mean of the distribution of values from 0.

SNF clustering

For boundaries (RobusTAD and Insulation Score) and compartments (eigenvector), feature scores were first filtered to include only positions where <5% of samples resulted in undefined calls and positions that were among the top 40% of variance across samples. Inter-sample distances were then calculated using the squared Euclidean distance as recommended by the SNF manual for continuous values.

For domain calls (Arrowhead and TADpole) and loop calls (HiCCUPS, Mustache, and Chromosight), the numerical values of the feature scores were found to be noisier than the binary presence or absence of the feature call, therefore the Jaccard distance between called features was used. For contact matrices overall, HiCRep[80] was used to calculate the Stratum-adjusted Correlation Coefficient (SCC), and distance between samples was taken as (1 – SCC).

Next, the affinity matrix for each feature was calculated with K = 20 and sigma = 0.3. The overall fused matrix between these affinity matrices was calculated with K = 20 and T = 16. The distance between samples was taken as (0.5 – similarity). Finally, these distances were plotted using UMAP with n_components = 2. Concordance of individual features with the final fused matrix were generated using concordanceNetworkNMI with C = 2. Distance between annotated features was taken as (1 – concordance).

Feature enrichment analyses

Overlap between either up- or down-regulated loop anchors and the Ensembl regulatory build annotations v20190329[84] using a Fisher's exact test, with the background set being the complete set of loop anchors across all ependymoma samples.

Motif enrichment within TULIPs was computed as the motif density 1-kb bins for TULIPs (and flanking regions) normalized to a background of shuffled intervals matching in GC and simple repeat content. Null regions, equal in number to the observed regions, were generated using genNullSeqs from gkmSVM v0.81.0[60] using default parameters and performed separately for TULIPs and flanking regions. Aggregate plots centered on TULIPs were then produced using the computeMatrix module from deepTools v3.5.1.[61]

Repeat element enrichment within TULIPs was compared against conserved compartment B regions defined as 50-kb bins with a negative score in at least 10 PFA samples. The significance of overlap with RepeatMasker annotations were assessed using Fisher's exact tests.

The web-based g:GOST module of g:Profiler with default parameters was used to assess pathway over-representation within gene lists of interest.

3D modeling of genome-wide contacts

1000 whole-nucleus structures per sample were simulated at 1Mb resolution using IGM commit bcea032 (https://github.com/alberlab/igm,[85]) with default parameters. The mean pairwise distance between TULIP regions was then computed for each model, providing 1000 values per sample. Structures were visualized using VMD v1.9.3.[56]

Transcriptome analysis

Library preparation

RNA-Seq libraries were generated and sequenced at Ontario Institute for Cancer Research (OICR) using Kapa RNA HyperPrep kit. Three RNA-Seq libraries were pooled per lane of HiSeq 2500 High-output PE126.

Differential expression

RNA-seq reads were aligned to hg38 (GCA_000001405.15_GRCh38_no_alt_plus_hs38d1_analysis_set) using HISAT2 (v2.1.0)[62] with parameters '–rna-strandness RF –downstream-transcriptome-assembly'. SAM output was sorted, converted to BAM, and indexed using samtools (v1.9).[63] A counts table was prepared using the count function of HTSeq (v0.13)[64] and differential expression testing was performed using Limma with Voom transformation (v3.44).[65]

De novo transcript analysis

StringTie (v2.0) was used to annotate transcripts present in each sample[66,67] using parameters '-m 150', then 'stringtie –merge' was used to generate a unified annotation GTF. GffCompare (v 0.11.7)[68] was run to determine how each of our *de novo* annotations compared to the GENCODE reference (v34).[86] FASTA sequences for each transcript were extracted using GffRead (v0.11.7).[68] RNA-seq reads were pseudoaligned and quantified using kallisto (v 0.45.1).[69] Strand-specific RNA-seq coverage tracks were generated from the HISAT2 aligned BAMs using deepTools (v3.5.1)[61] bamCoverage with parameters '–effectiveGenomeSize 2913022398 –normalizeUsing RPGC –binSize 1' and either '–filterRNAstrand forward' or '–filterRNAstrand reverse'. Overlap between genes, transcripts, superenhancers, and TULIPs was performed using bedtools intersect.

Comparison RNA-seq

This study makes use of data generated by the St. Jude Children's Research Hospital – Washington University Pediatric Cancer Genome Project. RNA-seq count matrices spanning ependymoma,[87] high-grade glioma[88] and medulloblastoma were accessed from the St. Jude Cloud.[89]

Bulk RNA-seq deconvolution

Reference single-cell RNA-seq and cell assignments were accessed.[90] Additionally, non-tumor cell identities were assigned using CellAssign (v0.99).[70] Bulk RNA-seq data was deconvoluted using CIBERSORTx[71] with batch correction and 1000 permutations.

Differentially methylated regions

Differentially methylated regions (DMRs) in PFA were obtained from Mack et al., 2014.[2] Genome coordinates were converted from hg19 to hg38 with UCSC liftOver. Bedgraphs of DMRs and the differential methylation values were converted to BigWig using UCSC bedGraphToBigWig.

Aggregate plots of DMRs overlapping TULIPs were generated using deepTools. First, computeMatrix was called with parameters 'scale-regions –regionBodyLength 1000000 –binSize 25000 –upstream 1000000 –downstream 1000000 –averageTypeBins "sum" –missingDataAsZero'. Then plotHeatmap was used with parameters '–colorList "blue, white,yellow" –sortRegions ascend –zMin −0.50 –zMax 0.50' for the final plots.

Aggregation of DNA methylation

Raw reads of whole-genome bisulfite sequencing (WGBS) were submitted to Bismark (v0.22.3)[72] for mapping and methylation calling, discarding duplicate reads. CpGs that overlapped with SNPs from dbSNPs or were located within the ENCODE blacklisted regions were excluded and only CpGs covered by $\geq 5\times$ were retained for the computation of DNA methylation levels. The aggregate plots and heatmaps of DNA methylation were generated using deepTools v3.1.0.[61] We used bedGraphToBigWig to generate bigwig files, then applied computeMatrix (scale-regions –regionBodyLength 5000000 –beforeRegionStartLength 5000000 –afterRegionStartLength 5000000 –binSize 50000 –skipZeros) to obtain enrichment matrices around TULIPs. After that, enrichment matrices were visualized in heatmaps using custom scripts, and aggregate plots were produced by averaging the score in bins across rows from the enrichment matrices.

Super-enhancers (SEs)

H3K27ac ChIP data from PFAs was accessed from[42] as hg19-aligned BAMs. MACS2[79] was used to call both broad and narrow peaks using parameters '–gsize hs –bdg –SPMR'. ROSE[34,35] was used to call SE regions from broad peaks using parameters '-s 6000 -t 2500'. CREAM (v1.1.1)[91] was used to call SE regions from narrow peaks using parameters 'MinLength = 1000, peakNumMin = 2'. We considered the union of ROSE and CREAM calls to be SE regions. Genome coordinates were converted from hg19 to hg38 with UCSC liftOver. Finally, we defined recurrent PFA SEs as those that were detected in 2 or more PFA samples.

Please cite this article in press as: Johnston et al., TULIPs decorate the three-dimensional genome of PFA ependymoma, Cell (2024), https://doi.org/10.1016/j.cell.2024.06.023

ChIP-seq

Library preparation

ChIP-seq was performed as previously described for primary cultures[11] and tumor tissue.[42] The H3K9me3 antibody (5 μg, Active Motif, 39161) was applied to both primary cultures and tumor tissue. Diagenode H3K27me3 antibody (5 μg, C15410069) was applied to tumor tissue samples, while Cell Signaling Technology H3K27me3 antibody (3 μg, CST 9733) was applied to primary cultures. Libraries were generated using Kapa HyperPrep kit (Roche, KR0961) and sequenced on the NovaSeq 6000 PE50.

Peak calling

Reads were aligned using using bwa mem to hg38 coordinates (GCA_000001405.15_GRCh38_no_alt_plus_hs38d1_analysis_set). Alignments were filtered out if (1) the chromosome name contained ''chrUn'', ''random'', or ''_alt'' (2) the alignment MAPQ was lower than 30 or (3) the alignment overlapped the ENCODE Unified GRCh38 Exclusion List (https://www.encodeproject.org/files/ENCFF356LFX/). Peak calling was performed using MACS2 (v 2.1.2) including input control BAMs. Additional parameters to the MACS2 callpeak function include: ''-f BAMPE -g hs –broad –bdg –SPMR''. Fold enrichment traces were generated using MACS2 bdgcmp with the parameter ''-m FE''.

Signal aggregation

For aggregate signal analysis, ChIP coverage was normalized using deepTools (v3.5.1) bamCoverage with parameters: ''–binSize 10 –normalizeUsing CPM –effectiveGenomeSize 2750000000 –extendReads –ignoreForNormalization chrX chrY chrM''. ChIP signal was aggregated over the recurrent TULIP BED positions using the deepTools function ''computeMatrix scale-regions'' with parameters: ''–regionBodyLength 1000000 –binSize 25000 –upstream 1000000 –downstream 1000000 –missingDataAsZero –averageTypeBins mean''. Scaled ChIP signal was then plotted using plotHeatmap.

Feature association

To assess the association between TULIPs and H3K9me3, wide spans of H3K9me3 peaks were identified by using ''bedtools merge -d 25000'' to unite near-adjacent regions, and then filtering for regions larger than 250 kb. Significance testing for overlap between these wide spans of H3K9me3 and TULIPs used Fisher's exact test, as implemented by bedtools fisher. Association between wide spans of H3K9me3 and TULIPs was further tested using bedtools reldist. Significance testing used the Student's t test to compare if the observed frequency of observations at a relative distance of zero (overlapping) was greater than the expected value of 0.02 for unassociated features.

NMF dimension reduction was run with library NMF (v0.21.0) in R 3.6.3. RobusTAD was run with library optparse (v1.6.6) in R 3.6.3. Visualization of Hi-C contacts and annotated features was performed using Juicebox (v1.11.08),[81] HiCExplorer (v3.7.2),[74] pyGenomeTracks (v3.6)[75] or IGV (v2.12.3).[76]

Oxford nanopore long-read sequencing

High molecular weight DNA was extracted using the Nanobind Tissue Big DNA Kit (Circulomics, Baltimore, Maryland, United States, NB-900-701-01) following the Mammalian Brain Application Note v1 (12–2019). DNA yields were measured by Qubit dsDNA BR Assay Kit (ThermoFisher Scientific, cat# Q32853) and molecule length was assessed by Femto Pulse (Genomic DNA 165 kb Kit, 3 h run, Agilent Technologies, Inc., Santa Clara, California, United States, cat# FP-1002-0275). Size selection was done using the Short Read Eliminator Kit (Circulomics, Baltimore, Maryland, United States, SS-100-101-01) as needed and DNA quality was reassessed as above. Libraries were prepared using the Ligation Sequencing Kit as per protocol (Oxford Nanopore Technologies Ltd, Oxford Science Park, Oxford, United Kingdom, SQK-LSK110) and sequenced on one (samples E519 and E820) or two (samples E833 and EPT838) PromethION flow cells (Oxford Nanopore Technologies Ltd, Oxford Science Park, Oxford, United Kingdom, FLO-PRO002). Base calling was done with Guppy version 4.0.11 and sample were aligned to GRCh38 using minimap2 with the following parameters *-ax map-ont*.[77] Quality control metric where generated using PycoQC (https://github.com/tleonardi/pycoQC). The N50 for aligned reads was between 9.3 and 46.1kb and the median aligned read length ranged from 2990 bp-9690 bp. Total genome coverage ranged from 22.3X-44.4X per sample. Structural variants were called using SVIM version 1.2.0 and required a minimum MAPQ score of 7.[78] Bedtools intersect was used to find structural variants overlapping TULIP regions.

OncoPrint

OncoPrint display for mutations in genes involved in 3D genome conformation in pediatric CNS tumors was generated using Pediatric Brain Tumor Atlas (PBTA) provisional data (852 patients, 1037 samples) accessed through PedcBioportal (https://pedcbioportal.kidsfirstdrc.org).

Immunohistochemistry of primary tumors

FFPE slides of primary tumors (2 PFA, 2 PFB, 1 medulloblastoma) were obtained from the Charbonneau Cancer Institute Brain Tumor Tissue Bank (University of Calgary). Slides were deparaffinized and dehydrated, then treated with antigen retrieval in EDTA buffer pH 8 with 0.05% Tween in a pressure cooker. Slides were blocked in PBS +0.5% BSA with 0.1% Triton X-100 and primary antibody (Rabbit anti-H3K9me3; Abcam ab8898) was applied overnight at 4 C. Washes were performed in PBS +0.1% Triton X-100. Secondary antibody staining was performed for 1 h at room temperature (Invitrogen Goat anti-rabbit Alexa 647; A-21245). Slides were washed and counterstained with DAPI at 1 μg/mL (Thermo Fisher 62248) and mounted with #1.5 glass coverslips (Globe Scientific) using FluorSave mountant (EMD Millipore). Images were acquired in the Charbonneau Microscopy Facility (University of Calgary) on a Zeiss LSM 880 with Airyscan detector. Final images were generated using ImageJ.

Immunocytochemistry

Cells were plated on 12 mm German glass coverslips (89167-106, VWR) coated with poly-L-ornithine (P4957, Sigma-Aldrich) and laminin (L2020, Sigma-Aldrich), for 24 h. Cells were fixed in 4% PFA in PBS for 10 min at room temperature. Coverslips were blocked in 5% BSA in PBS with 0.1% Tween for 1 h at room temperature. Staining was performed overnight at 4°C.

Primary antibodies used

Rabbit Anti-Histone H3 (tri methyl K9) antibody - ChIP Grade (dilution 1:1000; ab8898, Abcam), goat Anti-HP1α antibody - ChIP Grade (dilution 1:1000; ab77256, Abcam), Mouse HP1γ Monoclonal Antibody (2MOD-1G6, Thermo Fisher) at 1:250 dilution.

Secondary antibody staining was performed for 1 h at room temperature using fluorescently conjugated secondary antibodies

Donkey anti-Rabbit IgG (H + L), Alexa Fluor 647, (dilution 1:500; A31573, Thermo Fisher), Donkey anti-goat IgG (H + L), Alexa Fluor 647, (dilution 1:500; A21447, Thermo Fisher),Goat anti-Mouse IgG (H + L) Cross-Adsorbed Secondary Antibody, Alexa Fluor 488 (dilution 1:500; A-11001, Thermo Fisher). Samples were incubated for 5 min in DAPI (dilution 1:1000; 62248, Thermo Fisher). Washes were performed using PBS with 0.1% Tween and mounted with Prolong Diamond antifade (P36965, Life Technologies). Images were acquired using the ZEISS LSM 880 Airyscan confocal microscope.

Western blot

Protein concentration of samples was determined using the DC (detergent compatible) protein assay (5000112, Bio-Rad). Samples were prepared in a total volume of 20 μL at 10 μg/μL in Laemmli loading buffer. Samples were run on 10% Mini-PROTEAN gels (4568044, Bio-Rad) or 12% Mini-PROTEAN gels (4568045, Bio-Rad).

Primary antibodies used: Rabbit anti-EZHIP polyclonal antibody (ABC1378, Millipore), Rabbit Anti-Histone H3 (tri methyl K9) antibody - ChIP Grade (ab8898, Abcam), H3K27me3 monoclonal antibody (C15410069, Diagenode), at 1:1000 and Histone H3 K27Ac Antibody (39134, Active Motif) at 1:500 dilution.

Secondary antibodies used: Goat anti-rabbit IgG H&L (hrp) (ab6721, Abcam) at 1:20000.

Proliferation EdU assay

$2*10^4$cCells were plated on chambered 18 Well μ-Slide Glass Bottom (81817, ibidi) coated with poly-L-ornithine (P4957, Sigma-Aldrich) and laminin (L2020, Sigma-Aldrich), for 24 h. ClickIT Plus EdU Cell Proliferation, Alexa Fluor 647 Imaging Kit (C10640, Thermo) was used according to manufacturer's instructions. Briefly, cells were cultured with EdU for 4 h to allow incorporation of fluorescently labeled EdU into newly synthesized DNA therefore marking the proliferating cells. Cells were then fixed, permeabilized and labeled with ClickIT-647. Then incubated for 5 min in DAPI (dilution 1:1000; 62248, Thermo Fisher), washed in PBS, and mounted with ibidi mounting medium (50001, ibidi). Images were acquired on the ZEISS LSM 880 Airyscan confocal microscopy.

1,6-Hexanediol treatment

Cells were grown on 12 mm German glass coverslips (VWR 89167-106) coated with poly-L-ornithine (P4957, Sigma-Aldrich) and laminin (L2020, Sigma-Aldrich), and treated with 0%, 3%, and 10% (w/v) 1,6-hexanediol (240117-50G, Sigma-Aldrich) for 5 min. Cells were fixed in 4% PFA in PBS for 10 min at room temperature. Coverslips were blocked in 5% BSA in PBS with 0.1% Tween for 1 h at room temperature. Staining was performed overnight at 4°C with the Rabbit Anti-Histone H3 (tri methyl K9) antibody - ChIP Grade (ab8898, Abcam), at a dilution of 1:1000, followed by labeling with Donkey anti-Rabbit IgG (H + L), Alexa Fluor 647, (dilution 1:500; A31573, Invitrogen) for 1 h in the dark and then incubated for 5 min in DAPI (dilution 1:1000; 62248, Thermo Fisher). Washes were performed using PBS with 0.1% Tween. and mounted with Prolong Diamond antifade (P36965, Life Technologies). Images were acquired using the ZEISS LSM 880 Airyscan confocal microscope.

Fluorescence *in situ* hybridization

Probe design

Custom oligo-FISH probes were designed against three compartment B regions (chr8:34200000–35500000, chr8:394500000–39800000, chr8:43250000-43750000) and two compartment A regions (chr8:3775000–38450000, chr8:41500000-42050000) (myTags, Arbor Biosciences), and tagged with ATTO-647 and Alexa 488 respectively.

Pretreatment of Formalin-fixed Paraffin-embedded (FFPE) tissue

FFPE slides of primary tumors (2 PFA, 2 PFB) were obtained from the Charbonneau Cancer Institute Brain Tumor Tissue Bank (University of Calgary). Sample preparation was based on a previously published protocol.[92] In brief, slides were incubated in a hybridization oven at 56°C for an hour, deparaffinized and dehydrated. Slides were then treated with 0.1 N HCl at room temperature for 20 min. Antigen retrieval was performed with a citrate buffer (pH 6) for 30 min in a pressure cooker. Tissue was then treated with proteinase K (20 μg/mL) for 15 min at 37°C. Slides were then dehydrated and air dried.

Pretreatment of primary PFA cells

After treatment with drug compounds (1 mM UNC0642, 1 mM A366) for 7 days, cells were harvested with Accutase (Stem Cell Technologies) and resuspended in PBS. Slides were spun down onto charged slides using a Shandon CytoSpin 4 centrifuge (Thermo) at low speed, 400 RPM, for 3 min and fixed in 4% PFA. Cells on slides were permeabilized with 0.5% Triton X-100 in PBS for 10 min, and rinsed in PBS. They were then incubated for 20 min with 20% glycerol in PBS, followed by 3 rounds of brief snap-freezing and thaws in

liquid nitrogen, followed by two PBS washes. Slides were then incubated in 0.1 N HCl for 5 min, washed in PBS, and incubated again for 5 min in 2x SSCT and 50% formamide.

Probe hybridization

Hybridization mixture (50% formamide, 2x SSC, 1% Tween 20, 10% dextran sulfate, 1x Denhardt's solution) containing 20 pmol of each probeset was added to slides, sealed with rubber cement, and denatured at 81 C for 10 min, then incubated overnight in the dark at 37 C. Cytospin samples were washed with 2xSSCT at 60 C × 15 min, followed by 2xSSCT wash for 10 min at room temperature, and 0.2X SSC wash at room temperature for 10 min. FFPE samples were washed for 3 min in 0.4x SSC +0.3% NP-40/Igepal. Slides were costained with DAPI in 2x SSC (1:1000) for 5 min, and rinsed in 2x SSC. Slides were mounted with #1.5 glass coverslips (Globe Scientific) using FluorSave (EMD Millipore) and dried.

Image acquisition and analysis

Imaging was performed in the Charbonneau Microscopy Facility (University of Calgary) on a Zeiss LSM 880 with Airyscan detector. Images were taken as Z-stacks at 600x, with at least two Z-stacks imaged per slide, and further analyzed using ImageJ. Prior to particle analysis of individual foci, deconvolution was performed using the Diffraction PSF 3D plug-in, followed by the Parallel Spectral Convolution 3D plugin with a Generalized Tikhonov method, and a regularization parameter of 0.0008. Following this, maximum intensity projections were generated, images were thresholded and particles were identified using the Analyze Particles tool in ImageJ. These 2D analyses were then analyzed and visualized using custom R scripts. For 3D analyses, images were identified using the 3D object counter plugin and subsequent analysis was performed using custom R scripts.

Chemical inhibitors

Primary cells were plated on 96-well tissue-culture coated plates coated with poly-L-ornithine and laminin, at 2000 cells per well. Cells were treated with a gradient of doses of chaetocin (Cayman Chemical) and Alamar blue reagent (Thermo Fisher) was added after 24 h to assess cell viability. Plates were read on a spectrophotometer by measuring fluorescence at 590 nm.

Generation of EZHIP overexpression cultures

The pPB[Exp]-Puro-EF1A > hEZHIP [NM_203407.3] construct (VB220623-1246rfk, VectorBuilder) and pPB[Exp]-Puro-EF1A>TurboRFP (VB900129-0773jdw, VectorBuilder) were used to create a stable line using Piggybac transposase (PB210PA-1, System Biosciences). A total of 500,000 human neural progenitor cells were transfected using the mouse neural stem cell nucleofection kit (Lonza, VPG-1004) with 0.66 μg of the construct and 0.33 μg of transposase using the Lonza Amaxa Nucleofector I (protocol A-33), followed by selection with using 1.5 mg/mL puromycin after 48 h.

Transfection for wild type and mutant EZHIP overexpression experiments

The EF1a-EZHIP (WT)-turboRFP-Luc and EF1a-EZHIP (R405E)-turboRFP-Luc vectors were used. A total of 10^6 human neural progenitor cells were transfected using the mouse neural stem cell nucleofection kit (Lonza, VPG-1004) with 6 μg of the construct using the Lonza Amaxa Nucleofector I with protocol O-17, followed by selection with using 1.5 mg/mL puromycin after 24 h.

QUANTIFICATION AND STATISTICAL ANALYSIS

Data visualization was performed primarily in R (v4.0.3). Libraries used include broom (v0.7.5), hexbin (v1.28.2), ggpubr (v0.4.0), ggrepel (v0.9.1), RColorBrewer (v1.1.2), tidyverse (v1.3.0), and RIdeogram (v0.2.2).[73] Statistical details of experiments and analyses can be found in the text of the Results section and in the figure legends. Exact *p* values are provided for each analysis, unless they were exceedingly small (in which case *p* values were represented as a "lower-than" range).

CellPress
OPEN ACCESS

Supplemental figures

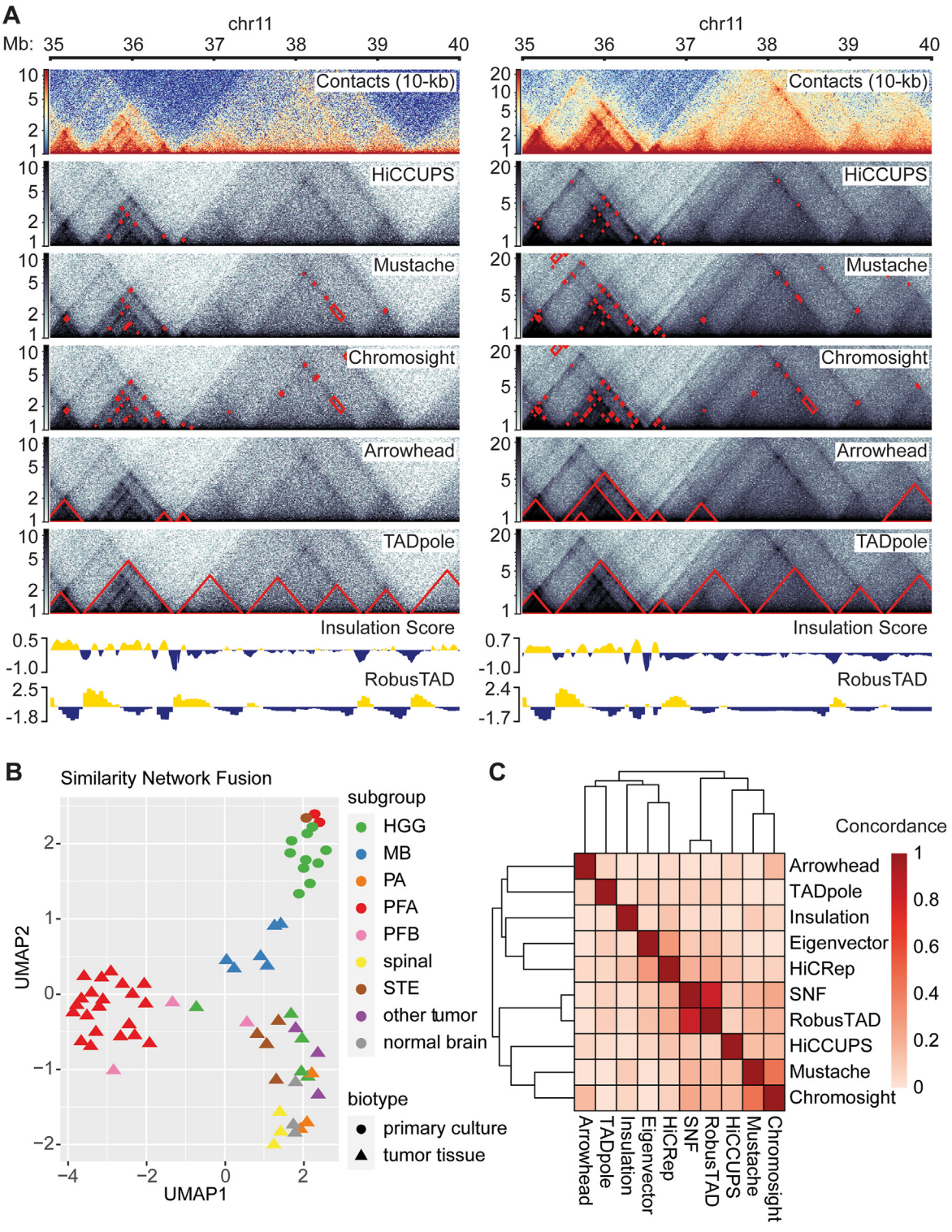

(legend on next page)

Figure S1. Segregation of tumor subgroups by 3D genome features, related to Figure 1

(A) Examples of downstream Hi-C feature annotations for a representative PFA (E2074, left) and PFB (E1859, right). Contact matrices show show a viewpoint at 10-kb resolution.

(B) UMAP projection of SNF affinity between samples including all analyzed feature annotations.

(C) Concordance between annotated 3D genome features and the SNF model. Concordance values closer to one suggest higher similarity. Distance between features was defined as one minus concordance. Rows were clustered based on the Euclidean distance between rows.

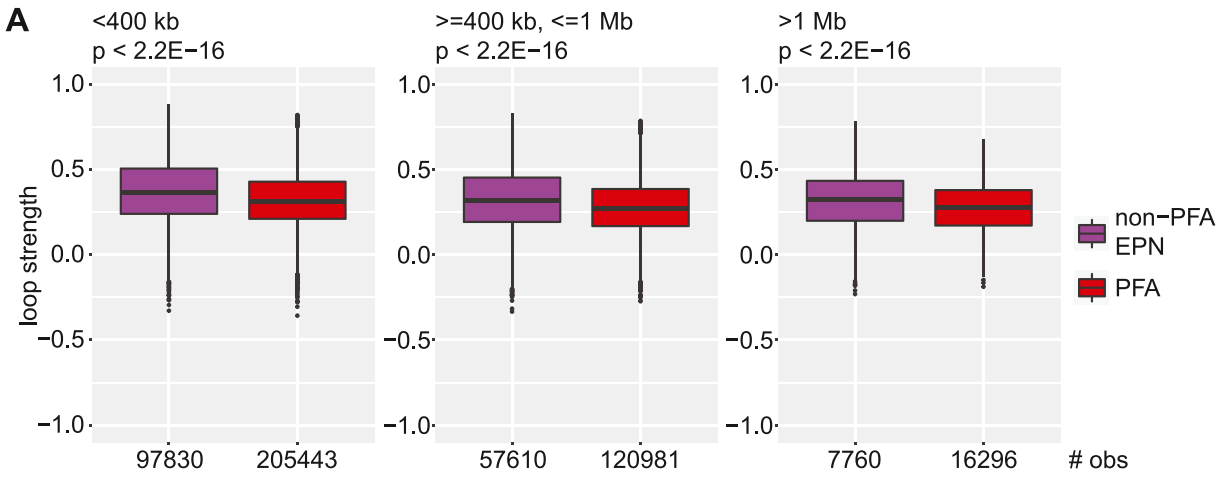

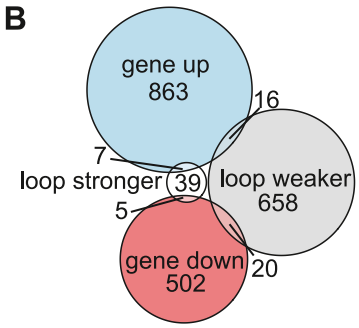

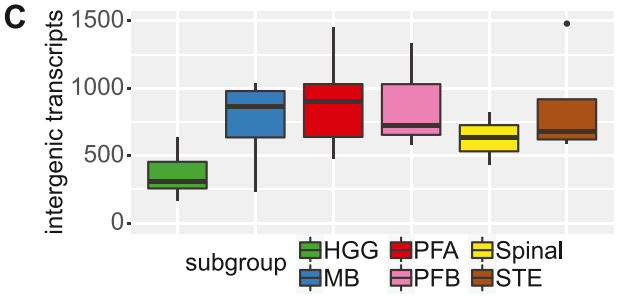

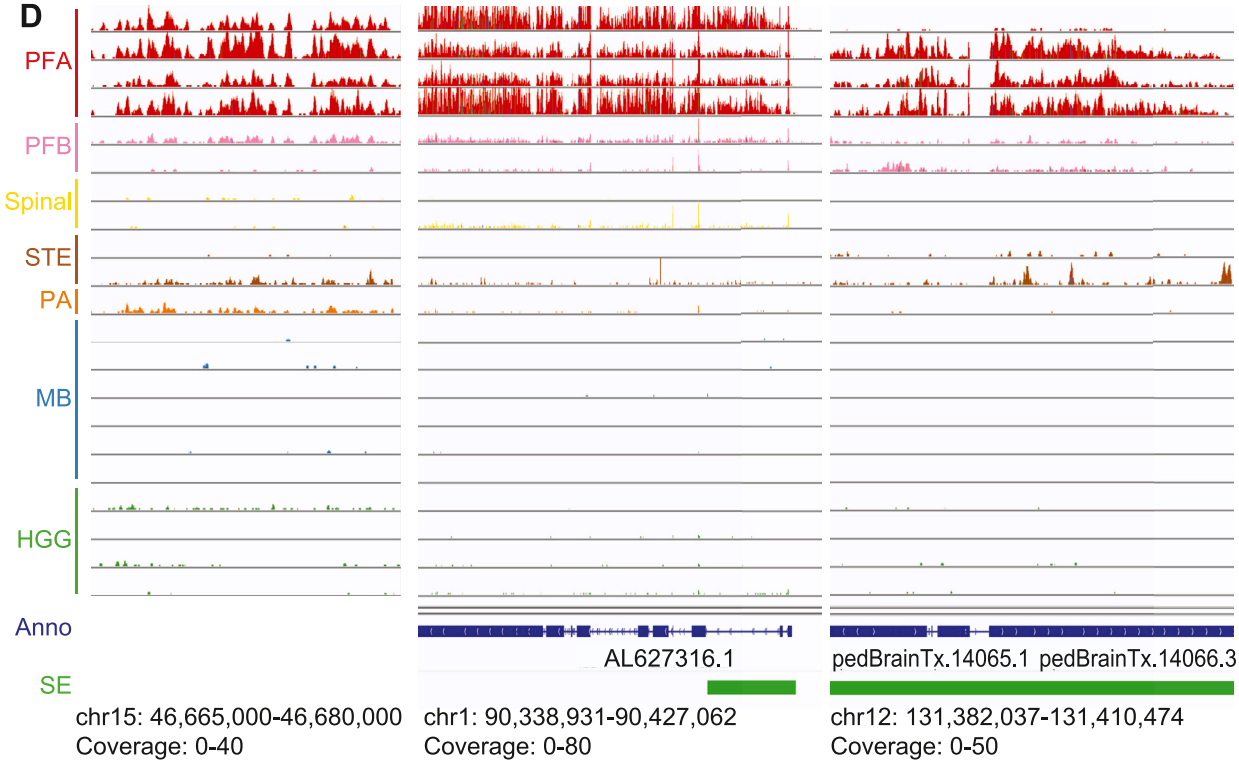

(legend on next page)

Figure S2. Differential loop strength and differential transcription in PFA tumors, related to Figure 2

(A) Global loop strength comparison between PFA and non-PFA EPN for the union set of Mustache-called loops, quantified by Chromosight, grouped by loop length. *P* values calculated using Wilcoxon rank-sum test.

(B) Euler plot displaying overlap between genes associated with differential transcription and differential loop interactions.

(C) Count of intergenic transcripts detected by StringTie RNA assembly with expression >1 TPM.

(D) RNA-seq coverage of loci containing PFA-enriched intergenic transcripts as well as overlapping gene annotations and super-enhancer calls.

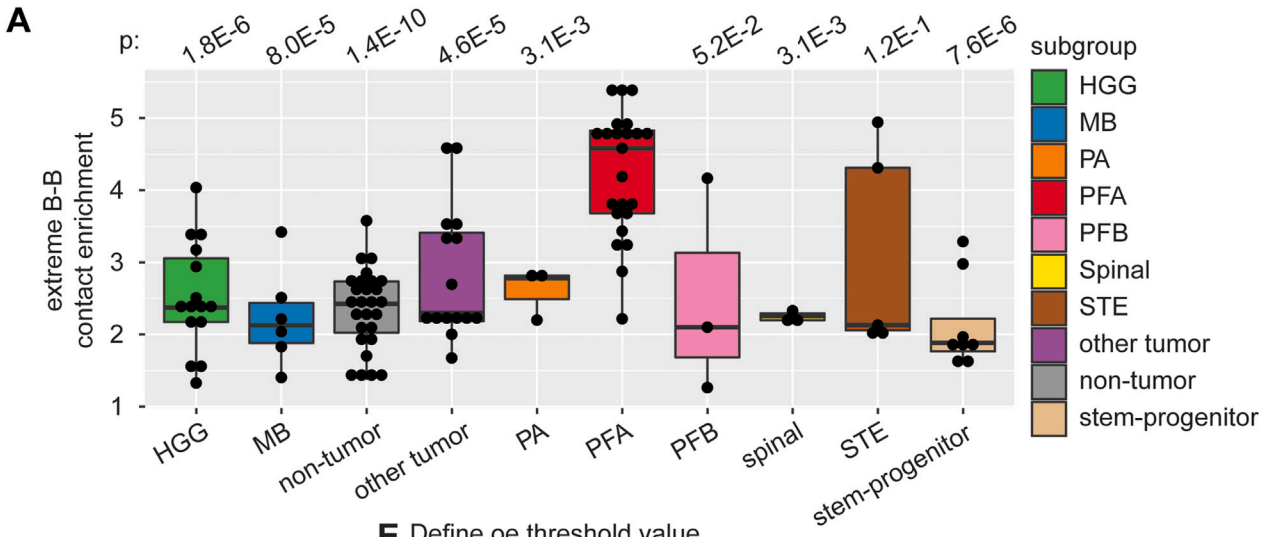

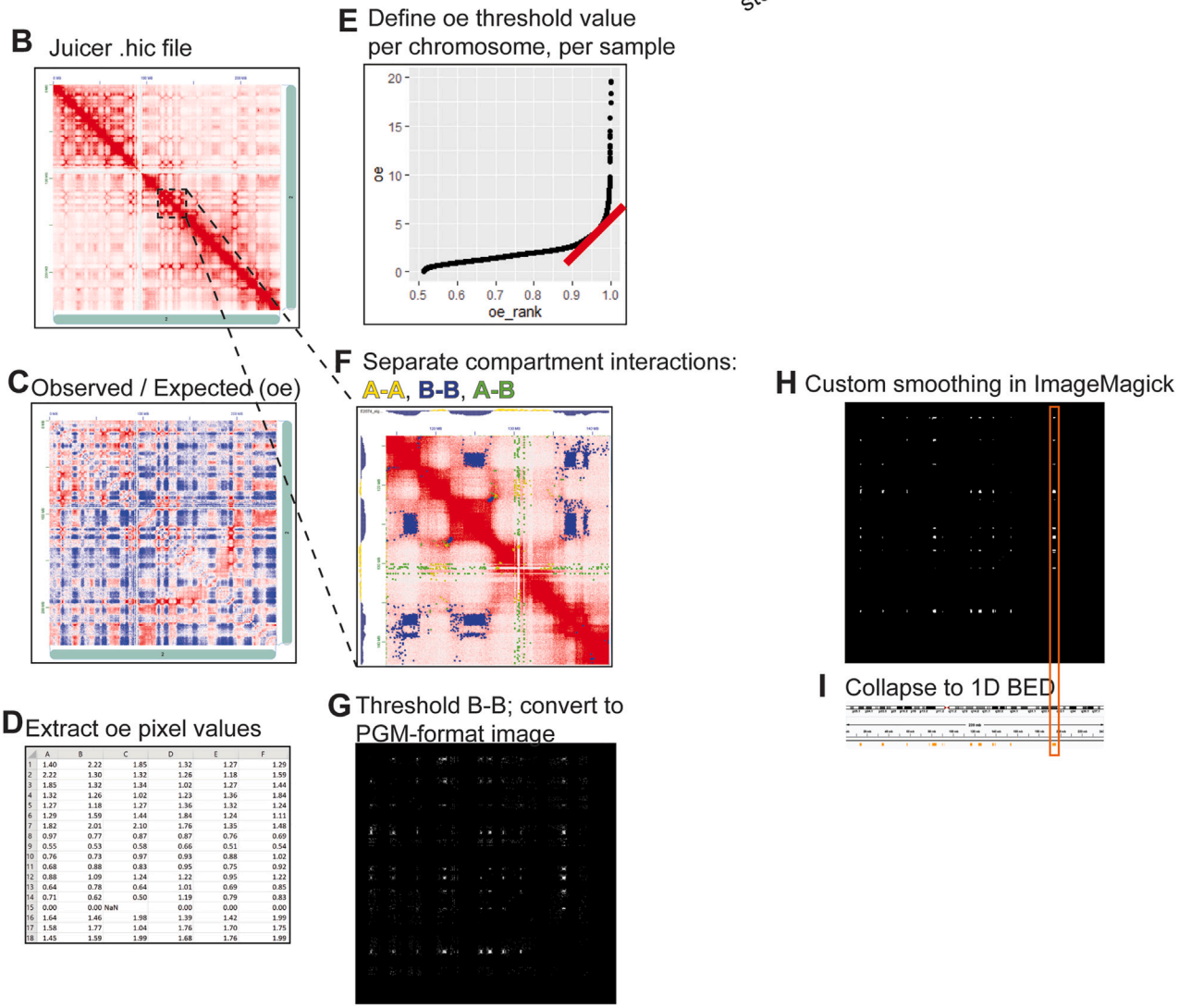

(legend on next page)

Figure S3. Distant B-B compartment interactions are strengthened in PFA, related to Figure 3

(A) Mean Obs/Exp values between genomic bins with the lowest 5 percent of compartment eigenvalues. Contacts separated by <10 Mb are excluded. *P* values calculated by Wilcoxon rank-sum test.

(B–I) Workflow for generating automated TULIP calls including: (B) Processed Hi-C contact matrix; (C) Observed/Expected ratio matrix; (D) Observed/Expected ratio values; (E) Threshold value detection; (F) Separation of pixels by compartment interaction type; (G) Conversion to PGM image; (H) Image smoothing with ImageMagick; (I) Collapse to 1D BED track.

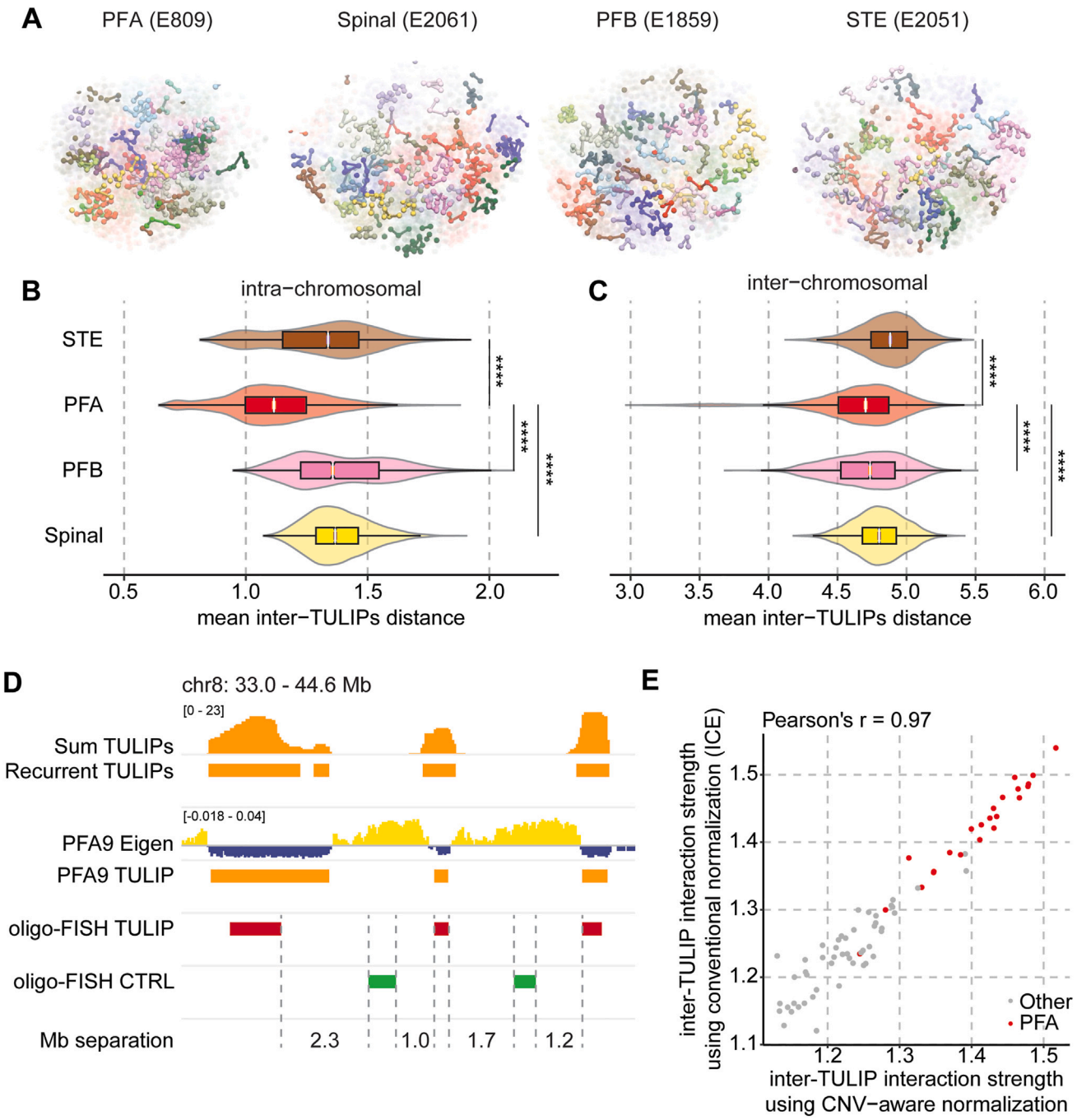

Figure S4. TULIPs are strongly associated with PFAs and are not structural rearrangements in the genome, related to Figure 4

(A) Representative 3D models of whole-nucleus, diploid chromosome conformation in PFA and non-PFA EPN. Bins along the same chromosome appear the same color. Recurrent TULIP loci appear opaque while non-TULIP loci appear translucent.

(B) Mean pairwise distance between intra-chromosomal TULIPs. Two-sided Wilcoxon rank-sum test $p < 2E\text{-}16$ for all comparisons.

(C) Mean pairwise distance between inter-chromosomal TULIPs. Two-sided Wilcoxon rank-sum test $p < 2E\text{-}16$ for all comparisons.

(D) Diagram summarizing the strategy for the design of oligo-FISH probes targeting 3 TULIPs and their intervening type A compartments along chromosome 8.

(E) Strength of inter-TULIP interactions observed using CNV-aware correction vs. without (ICE normalization).

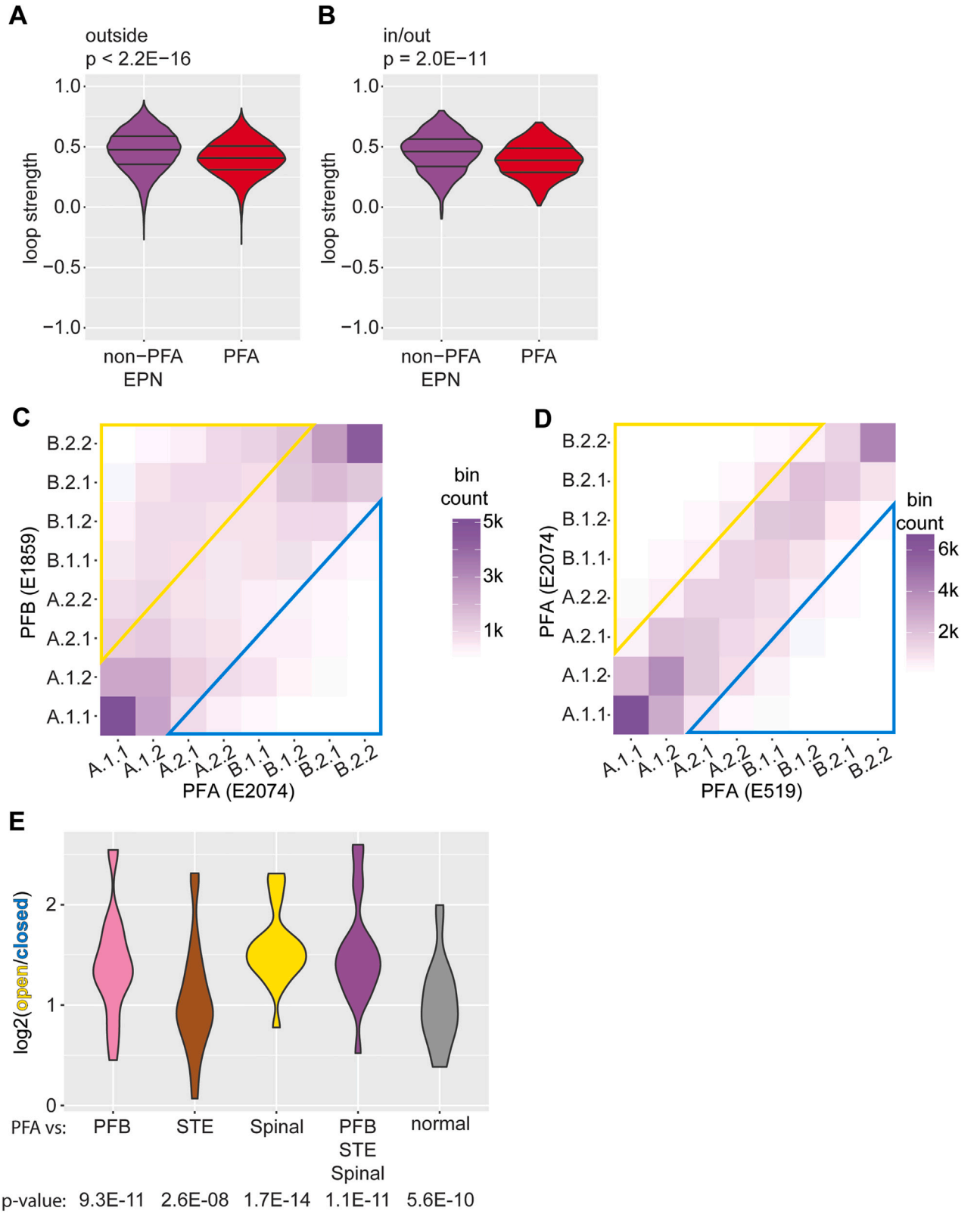

(legend on next page)

Figure S5. Influence of TULIPs upon 3D genome topology, related to Figure 5

(A) Comparison of interactions for loops with both anchors located outside of TULIPs in PFAs and non-PFA ependymoma (EPN). Distributions were compared using two-sided t tests. Horizontal lines indicate 25th, 50th, and 75th percentiles.

(B) Comparison of interactions for loops with one anchor located outside of TULIPs and one anchor located inside TULIPs in PFAs and non-PFA ependymoma (EPN). Distributions were compared using two-sided t tests. Horizontal lines indicate 25th, 50th, and 75th percentiles.

(C) CALDER comparison of genome compartmentalization between a PFB (E1859) and a PFA (E2074).

(D) CALDER comparison of genome compartmentalization between two PFA samples (E2074, E519).

(E) Summary of pairwise comparisons between individual PFA samples and subgroup-specific consensus compartmentalization. Two-sided t test with H_0: mean = 0 and H_1: mean $\neq$ 0.

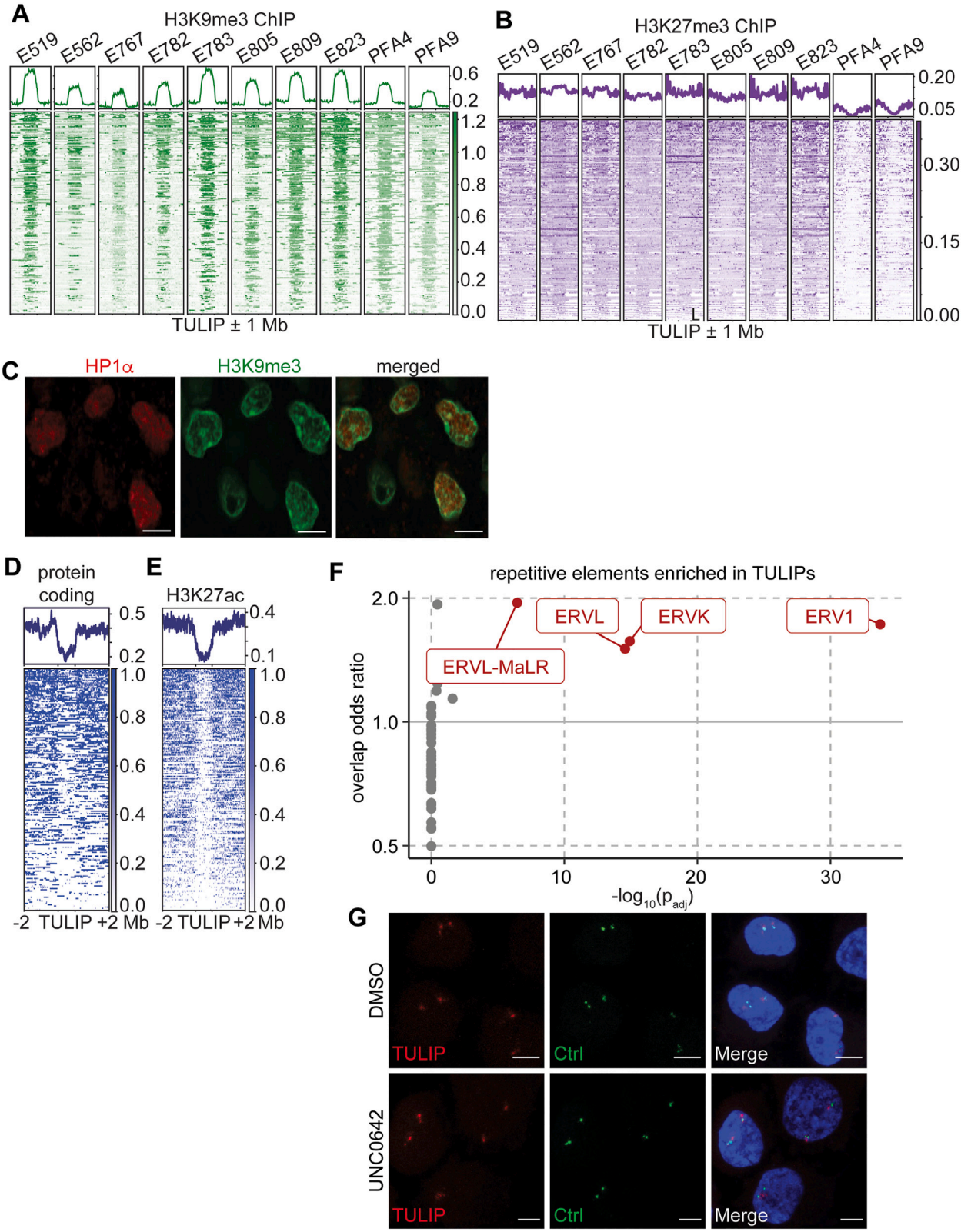

(legend on next page)

Figure S6. Epigenetic features of TULIPs, related to Figure 6

(A) Pileup analysis for H3K9me3 at TULIP regions in PFA samples.

(B) Pileup plots of H3K27me3 signal over recurrent TULIP loci for all PFA samples profiled.

(C) Immunofluorescence for HP1γ and H3K9me3 in a PFA surgical resection. Scale bar: 10 μm

(D) Pileup analysis for density of protein-coding genes at TULIP regions.

(E) Pileup analysis of H3K27ac signals across TULIPs and their surrounding regions in PFA samples.

(F) Repetitive element enrichment within TULIPs.

(G) Oligo-FISH experiment to detect TULIPs (red) or control (Ctrl) regions on chromosome 8 in PFA cells treated with DMSO or UNC0642.

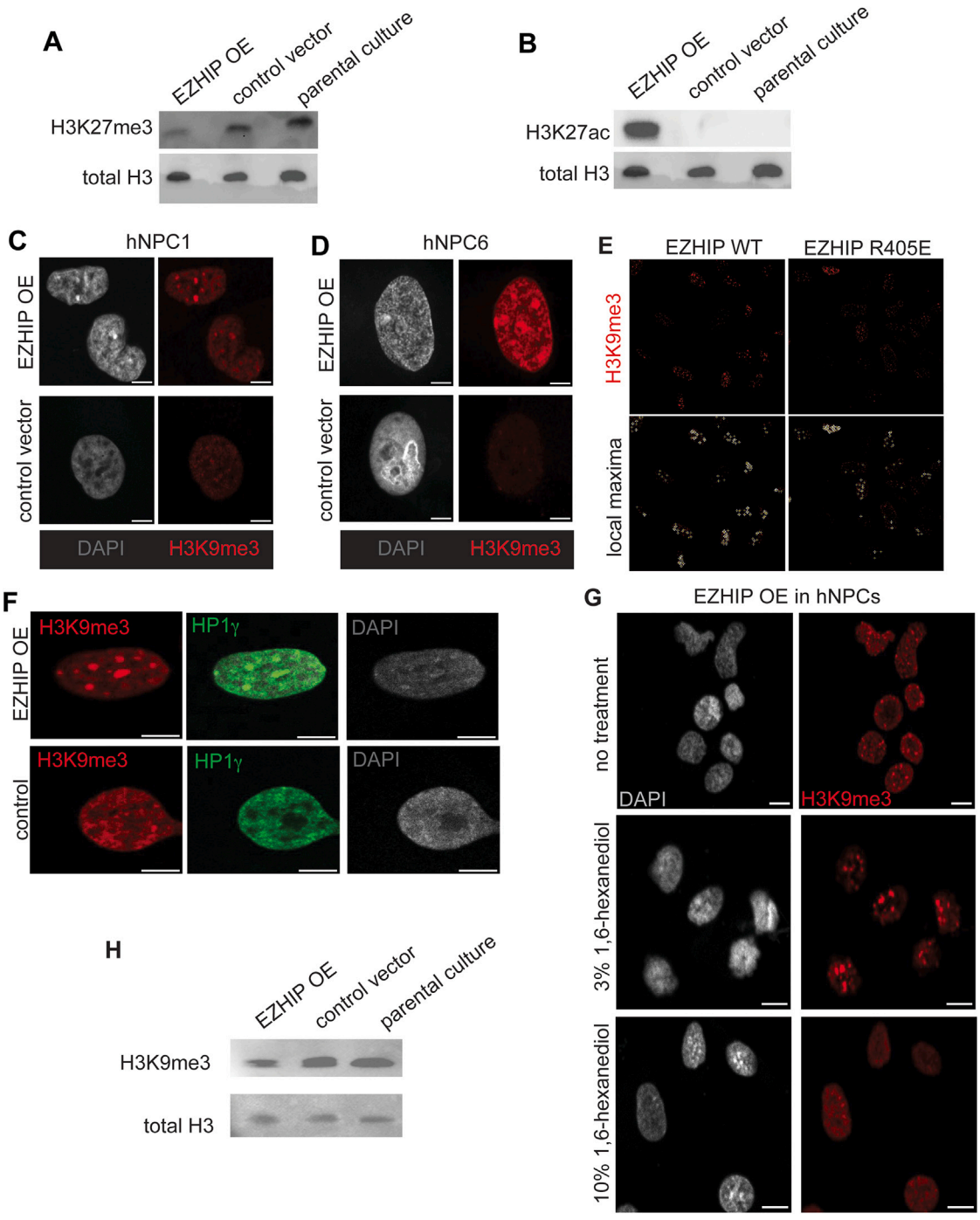

Figure S7. EZHIP mediates chromatin reorganization, related to Figure 7

(A) Western blot for H3K27me3 and total H3 with protein lysates prepared from hNPCs.

(B) Western blot for H3K27ac and total H3 with protein lysates prepared from hNPCs.

(C and D) Immunocytochemistry for H3K9me3 in hNPCs stably nucleofected with a vector for EZHIP overexpression (EZHIP OE) or with a control vector. The hNPC models are hNPC1 (C) and hNPC6 (D). Scale bar: 5 μm

(E) Immunocytochemistry for H3K9me3 in hNPCs expressing either wild-type EZHIP (EZHIP WT) or a mutant form (EZHIP R405E). ImageJ was used to determine the local maxima, as shown the in bottom row.

(F) Immunocytochemistry for H3K9me3 and HP1γ in control and EZHIP OE hNPCs. Scale bar: 5 μm

(G) Effects of 1,6-hexanediol on H3K9me3 foci in EZHIP OE hNPCs. Scale bar: 10 μm

(H) Western blot for H3K9me3 in hNPC models. Total H3 was used as a loading control.